ISSN 1063-780X, Plasma Physics Reports, 2022, Vol. 48, No. 3, pp. 242–262. © Pleiades Publishing, Ltd., 2022.
Russian Text © The Author(s), 2022, published in Fizika Plazmy, 2022, Vol. 48, No. 3, pp. 237–258.

SPACE PLASMA

Role of Oxygen Ions in the Structure of the Current Sheet of the Near-Earth Magnetotail

O. V. Mingalev[a, b, *], P. V. Setsko[a], M. N. Mel'nik[a], I. V. Mingalev[a, b, **], Kh. V. Malova[c, d, *], A. V. Artem'ev[d], A. M. Merzlyi[d], and L. M. Zelenyi[d]**

[a] Polar Geophysical Institute, Kola Scientific Center, Apatity, Murmansk oblast, 184209 Russia
[b] Murmansk Arctic State University, Apatity, Murmansk oblast, 184209 Russia
[c] Skobeltsyn Institute of Nuclear Physics, Moscow State University, Moscow, 119991 Russia
[d] Space Research Institute, Russian Academy of Sciences, Moscow, 117997 Russia
*e-mail: mingalev_o@pgia.ru
**e-mail: mingalev_i@pgia.ru
***e-mail: hmalova@yandex.ru

Received June 24, 2021; revised October 29, 2021; accepted November 10, 2021

Abstract—A numerical model is used to study the possibility of a thin current sheet formation in the near-Earth magnetotail in the growth phase of a substorm for a wide range of parameters of longitudinal counter-moving ion flows that create current sheet. The simulation results make it possible to conclude that the current sheet can be formed by oxygen ion flows of ionospheric origin in cases where the proton fluxes can be neglected or they are rather weak. Such conditions are realized in the Earth's magnetosphere during periods of increased geomagnetic activity. In addition, the influence of electron pressure anisotropy on the steady-state configuration of the considered current sheet is investigated.

Keywords: collisionless plasma, thin current sheets, substorm

DOI: 10.1134/S1063780X22030096

1. INTRODUCTION

The discovery of oxygen ion populations in the magnetosphere and the study of the mechanisms of their formation due to the outflow of ionospheric plasma raised the question of the influence of oxygen ions on the development of magnetospheric substorms and storms as the most important and powerful phenomena of magnetospheric dynamics. Researches in this direction has been developed since 1970s (see [1–5]), and the most complete review on this topic is done in the work [4].

One of the important mechanisms for the outflow of oxygen ions from the high-latitude ionosphere into the Earth's magnetosphere is the acceleration of ions by an ambipolar electric field. This field arises in the ionosphere and magnetosphere due to the small separation of charges and supports the quasi-neutrality of the plasma. It is determined from the condition of the longitudinal force equilibrium of electrons and is directed along the magnetic field lines oppositely to the electron pressure gradient, i.e. away from the Earth. In the conditions of increased geomagnetic activity in the electron precipitation regions, this field in the upper part of the F-sheet can increase by an order of magnitude due to an increase of the electron pressure. This leads to the fact that an oxygen ion population with a sufficiently high density appears in the plasma of the near Earth part of magnetosphere.

Important and not completely resolved issue of magnetospheric physics is the formation of a thin current sheet (hereinafter TCS) of the near-Earth magnetotail during periods of the increased geomagnetic activity (e.g., during the substorm growth phase) and its subsequent explosive destruction (see reviews [6, 7]). The stability and scenario of the current sheet (hereinafter CS) destruction mostly depends on its configuration before the decay. Experimental data and simulation results show that various quasi-stationary configurations of this TCS are possible; therefore, their study remains actual for recent decades.

It is known from experimental data that during the growth phase of substorm under geomagnetically active conditions, the contribution of oxygen ions to the total ion density in the plasma sheet increases from values on the order of 1–2% before substorms to values over 50% [2, 4, 8]. In the near Earth magnetosphere, oxygen ion flows directed from the Earth to the tail were detected on the force lines emerging from the high-latitude region of the ionosphere [4, 9–13]. The presence of current-carrying oxygen ions was repeatedly detected when the CS of the near-Earth tail was crossed by the CLUSTER missions in [2, 14]; oxygen ion fluxes entering the TCS of the near-Earth tail were detected.

Simulation and theoretical estimates show a significant dependence of the CS configuration on the parameters of the interpenetrating ion fluxes, which form it. Until recently, the parameters for the above oxygen ion fluxes were not directly measured and could only be approximately estimated, which reduced the value and reliability of simulation. In [15], the necessary data were obtained, and it was shown in the measurements of the THEMIS mission that oxygen ion O^+ fluxes of the ionospheric origin are observed in the plasma sheet directed to the magnetotail along magnetic field lines, which reach the magnetotail current sheet at distances of approximately $20R_E \le -x \le 40R_E$ (R_E is the radius of the Earth), and the longitudinal velocity of these fluxes in a significant part of the cases lies within $V_{DO} \sim 100–250$ km/s.

Experimental data show [1–5, 15] that the characteristic temperature of oxygen ions is hundreds of eV: $T_O \sim 0.1–0.9$ keV and less than the electron temperature T_e, which has a characteristic value on the order of 1 keV in the plasma sheet of the near-Earth tail, and the proton temperature usually lies in the range $T_p = 4–10$ keV. It follows that gyroradii of O^+ ions R_{cO} and protons R_{cp} are comparable:

$$R_{cO}/R_{cp} = \sqrt{(m_O T_O)/(m_p T_p)} \approx 4\sqrt{T_O/T_p} \sim 0.4–2.$$

We note that thermal velocities of oxygen ions $V_{TO} = \sqrt{eT_O/m_O}$ and protons $V_{Tp} = \sqrt{eT_p/m_p}$ (where e is the proton charge, and temperatures are expressed in eV) for temperatures from the above ranges lie approximately within $V_{TO} \approx 25–75$ km/s and $V_{Tp} \approx 619–980$ km/s. Hence it follows that for oxygen ions the values of the dimensionless flow parameter $\delta_O = V_{DO}/V_{TO}$ lie in the range of $\delta_O \sim 3–10$, i.e., can be rather large.

It follows from the presented data that under geomagnetically active conditions at the growth phase of substorm, a situation is quite possible when counter fluxes of O^+ ions with the temperature of $T_O \sim 0.1–0.4$ keV and longitudinal hydrodynamic velocity $V_{DO} \sim 200–250$ km/s are observed near the neutral sheet of the near-Earth tail, and protons either have a small value of the flux parameter $\delta_p = V_{Dp}/V_{Tp} < 1$, where V_{Dp} is the longitudinal hydrodynamic velocity of the proton flux, or they are a background with $V_{Dp} = 0$ (i.e., their distribution function in the sheet and its vicinity in the velocity space has the form of a "cloud" with the zero longitudinal hydrodynamic velocity). This situation differs from the most studied scenario, when the CS of the near-Earth tail is formed by counterstreaming proton fluxes of the magnetospheric origin.

In this regard, the following question arises: can there be a TCS formed by oxygen ion fluxes with the temperature $T_O \sim 0.1–0.4$ keV, when proton fluxes are either absent, i.e., protons are the background, or proton fluxes are weak and carry a relatively small part of the current through CS? In a broader formulation, the answer to this question should show whether the oxygen ion fluxes can significantly affect the structure of TCS or form TCS, i.e., whether the populations of these ionospheric ions are important for the structure and dynamics of TCS at the growth phase of substorm?

To obtain the answer to this question, it is necessary to study three possible cases when TCS is formed by (1) proton fluxes with relatively low longitudinal velocities at small values of the flux parameter $\delta_p = V_{Dp}/V_{Tp} < 1$; (2) only oxygen ion fluxes; (3) oxygen ion fluxes and proton fluxes.

Let us note that, according to modern concepts based on satellite measurements, there is a population of background protons that cannot carry current, as well as a population of background electrons in the current sheet of the near-Earth tail of the magnetosphere. This current sheet can be formed either by counter longitudinal fluxes of magnetospheric protons, or similar oxygen ion fluxes from the ionosphere, or fluxes of both types. In addition to the background population of electrons, their counter fluxes can be also present in this current sheet.

In analytical and numerical TCS models, it is possible to formally take into account the background population of magnetized electrons. The formal taking into account the counter longitudinal electron fluxes leads to a strong complication of the model. Therefore, in existing models, the counter electron fluxes are taken into account approximately by introducing the anisotropy of the electron pressure at the edges of CS, i.e., formally, electrons are considered as a magnetized background, the contribution of which to the parameters CS can be described analytically.

To study possible TCS configurations, a new version of the numerical model of a steady-state spatially one-dimensional TCS with a given normal magnetic field component was developed. In the TCS model, it is formed by counter propagating longitudinal (along the magnetic field lines) fluxes of ions of one or several types, and electrons are magnetized and have a Maxwell–Boltzmann distribution function, while their counter longitudinal fluxes are formally absent.

In comparison to the initial version of the model described in [16], the new version introduces three significant improvements. First, several kinds of ions can be considered. Secondly, asymmetric formulations of the problem can be considered, in which the shear component of the magnetic field is allowed.

Third, an analytical expression for the current density of magnetized electrons is obtained, which makes it possible to find the relative contribution of electrons to the total current through CS. It follows from this expression that, within the spatially one-dimensional model for symmetric TCS, electrons contribute to the total current through CS only if they have finite pressure anisotropy at the CS edge.

As a result of simulation, steady-state TCS configurations were obtained for the tangential magnetic field component outside the sheet $B_{x0} = 20$ nT and its normal component $B_z = 2$ nT for a representative set of values of the longitudinal velocity of the incident flows, which are well within the range of experimental data.

One can conclude from the simulation results that TCS in the near-Earth tail under disturbed conditions can be formed by oxygen ion fluxes of the ionospheric origin with parameters from the above ranges, while protons are either a background or their fluxes are relatively weak and make a smaller contribution to the total current.

We also note that this work continues and refines works [17, 18], in which, using an approximate analytical model, steady-state TCS configurations were obtained taking into account the oxygen ions fluxes for the dimensionless parameters outside the sheet $n_{\mathrm{O}}/n_p = 0$, 0.1, 0.25, 0.5, 1 and $T_{\mathrm{O}}/T_p = 0$, 0.1, 0.25, 0.5, 1. In these works, it was shown that in the presence of oxygen ion fluxes, a significant expansion of the current sheet is possible, however, due to the absence of the then known experimental data, important versions of TCS configurations with strong oxygen ion fluxes, for which protons are either a background or their flows are weak, were not considered.

2. AMBIPOLAR ELECTRIC FIELD

We consider the formation of an ambipolar electric field in the ionosphere and in the magnetosphere due to a very small charge separation, which is directed from the Earth and pulls oxygen ions from the F-sheet of the high-latitude ionosphere into the magnetosphere, and then accelerates them.

The potential part of the large-scale electric field in the ionosphere and magnetosphere is determined from the condition of the longitudinal force equilibrium of electrons, which has the form [19–22]

$$\left(\mathbf{B}\cdot\frac{d_e\mathbf{u}_e}{dt}\right) = 0, \qquad \frac{d_e\mathbf{u}_e}{dt} = \frac{\partial\mathbf{u}_e}{\partial t} + (\mathbf{u}_e\cdot\nabla)\mathbf{u}_e,$$

where $\mathbf{B}(\mathbf{x},t)$ is the magnetic induction vector, $\mathbf{u}_e(\mathbf{x},t)$ is the hydrodynamic velocity of electrons, and $(\mathbf{U}\cdot\mathbf{V})$ here and below denotes a scalar product of vectors $\mathbf{U}$ and $\mathbf{V}$. For evaluative reasoning, collisions of electrons in the upper ionosphere and near-Earth magnetosphere can be neglected (note that this is done in numerical models of the ionosphere [20–22]). Then the condition for the longitudinal force equilibrium of electrons takes the form

$$-e\,n_e(\mathbf{B}\cdot\mathbf{E}) = \left(\mathbf{B}\cdot(\nabla\cdot\widehat{\mathbf{P}}_e)\right), \tag{2.1}$$

where $\mathbf{E}(\mathbf{x},t)$ is the electric field strength vector, $n_e(\mathbf{x},t)$ is the electron density, $\widehat{\mathbf{P}}_e(\mathbf{x},t)$ is their pressure tensor, which, taking into account the magnetization of electrons, has the form

$$\widehat{\mathbf{P}}_e = p_{e\perp}\hat{\mathbf{I}} + (p_{e\parallel} - p_{e\perp})\,\mathbf{b}\otimes\mathbf{b}. \tag{2.2}$$

Here, $\hat{\mathbf{I}}$ is the unit tensor, $p_{e\parallel}(\mathbf{x},t)$ and $p_{e\perp}(\mathbf{x},t)$ are the longitudinal and orthogonal electron pressures, $\mathbf{b}(\mathbf{x},t) = \mathbf{B}/B$ is the unit vector along the magnetic field, and $\mathbf{b}\otimes\mathbf{b}$ denotes the dyadic tensor formed by this vector. The following expression for the longitudinal electric field follows from Eqs. (2.1) and (2.2):

$$(\mathbf{b}\cdot\mathbf{E}) = -\frac{1}{en_e} \times \left((\mathbf{b}\cdot\nabla p_{e\parallel}) - (p_{e\parallel} - p_{e\perp})(\mathbf{b}\cdot\nabla\ln B)\right). \tag{2.3}$$

For evaluative reasoning, the electron pressure can be considered isotropic, since its anisotropy is relatively small. Then $\nabla\cdot\widehat{\mathbf{P}}_e = \nabla p_e$, and the latter formula takes the form

$$(\mathbf{b}\cdot\mathbf{E}) = -(\mathbf{b}\cdot\nabla p_e)/(e\,n_e). \tag{2.4}$$

Under disturbed conditions in the high-latitude ionosphere, due to previous ionization and heating by erupting energetic particles [23, 24], as well as due to heating by Alfvén waves [25], the ion and electron densities, as well as their temperatures, increase significantly. As a result, at the preliminary substorm phase in the polar ionosphere, the electron pressure $p_e = e\,n_eT_e$ is significantly higher than in calm conditions. It is known from experimental data that the electron pressure decreases with distance from the Earth due to a sharp decrease in density by orders of magnitude with a simultaneous slower increase in their temperature. Therefore, the electron pressure gradient ∇p_e is directed to the Earth, and the longitudinal electric field determined by formula (2.4) in the high-latitude ionosphere is directed from the Earth. Such a field moves oxygen ions along the magnetic field lines from the F-layer of the high-latitude ionosphere and accelerates them, and also moves electrons from the magnetosphere to the ionosphere.

3. NUMERICAL MODEL OF THE STEADY-STATE TCS

We denote the vectors of the Cartesian basis of the coordinate system as $\mathbf{e}_x$, $\mathbf{e}_y$, and $\mathbf{e}_z$, as well as the components of the coordinate vector: $\mathbf{x} = x\mathbf{e}_x + y\mathbf{e}_y +$

$z\mathbf{e}_z \in \mathbb{R}^3$, and velocity vector components $\mathbf{v} = v_x\mathbf{e}_x + v_y\mathbf{e}_y + v_z\mathbf{e}_z \in \mathbb{R}^3$. In the considered CS, the **Z** axis is directed across the sheet, the magnetic field has a given constant normal component $B_z \equiv \text{const}$ and self-consistent components $B_x(z)$ and $B_y(z)$, and the electric field has one self-consistent component $E_z(z)$

$$\mathbf{B}(z) = B_x(z)\mathbf{e}_x + B_y(z)\mathbf{e}_y + B_z\mathbf{e}_z,$$
$$\mathbf{E}(z) = E_z(z)\mathbf{e}_z = -\frac{d\varphi(z)}{dz}\mathbf{e}_z, \quad (3.1)$$

where $\varphi(z)$ denotes a scalar potential.

In the model outside the simulation region $\{|z| < L\}$ the magnetic field is considered to be constant, and the electric field is considered to be zero

$$\mathbf{B}\big|_{z\geq L} \equiv \mathbf{B}^{(+)}, \quad \mathbf{B}\big|_{z\leq -L} \equiv \mathbf{B}^{(-)}, \quad \mathbf{E}\big|_{|z|\geq L} \equiv 0. \quad (3.2)$$

Here and below, superscripts (+) and (–) denote the values of the function at the upper and lower boundaries of CS, respectively. If the **X** axis is chosen along the vector of the magnetic field variation when passing through the sheet

$$\mathbf{e}_x = \Delta\mathbf{B}/\Delta B, \quad \Delta\mathbf{B} = \mathbf{B}^{(+)} - \mathbf{B}^{(-)}, \quad \Delta B = |\Delta\mathbf{B}|, \quad (3.3)$$

the component $B_y(z)$ is a shear one, i.e., $B_y(z)$ can change inside sheet, but does not change when passing through the sheet, and the component $B_x(z)$ is a tangential one:

$$B_y(-L) = B_y(L), \quad \Delta B = B_x(L) - B_x(-L). \quad (3.4)$$

The sheet is produced by counter ion fluxes along the magnetic field lines. The distribution function $f_\alpha^{(\pm)}(z,\mathbf{v})$ of each type of ions in the incident plasma flows at the boundary of the calculation region is the Maxwell distribution with the hydrodynamic velocity $\mathbf{U}_\alpha^{(\pm)} = -\frac{z\mathbf{B}^{(\pm)}}{|z|\left|\mathbf{B}^{(\pm)}\right|}V_{D\alpha}^{(\pm)}$, which is directed along the magnetic field lines towards the sheet and has a $V_{D\alpha}^{(\pm)}$ value (different for each type ions)

$$f_\alpha^{(\pm)}(\mathbf{v}) = \frac{n_\alpha^{(\pm)}}{\left(V_{T\alpha}^{(\pm)}\sqrt{2\pi}\right)^3}\exp\left(-\frac{1}{2\left(V_{T\alpha}^{(\pm)}\right)^2}\left|\mathbf{v} - \mathbf{U}_\alpha^{(\pm)}\right|^2\right),$$
$$\frac{z}{|z|}\left(\mathbf{B}^{(\pm)}\cdot\mathbf{v}\right) < 0, \quad (3.5)$$

where $n_\alpha^{(\pm)}$ is the density, $V_{T\alpha}^{(\pm)} = \sqrt{eT_\alpha^{(\pm)}/m_\alpha}$ is the thermal velocity, and $T_\alpha^{(\pm)}$ is temperature (in eV) in these fluxes. The geometry of the problem is shown schematically in Fig. 1.

In the model the ion components are described by the steady-state Vlasov equations which are solved numerically using the method described in [16]. Magnetized electrons are described by the steady-state Vlasov equation in the drift approximation (see [16, 19, 26–30]), and their current density, according to the drift theory, is given by the formula

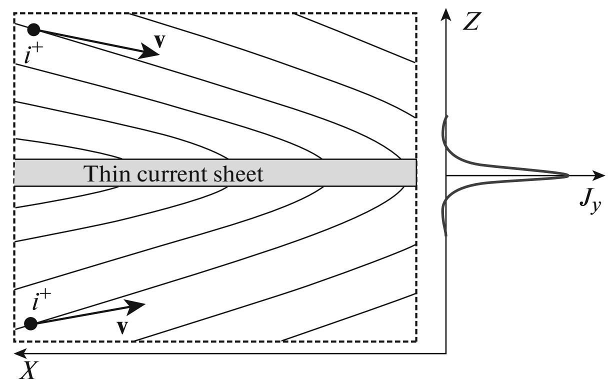

Fig. 1. Geometry of the problem.

$$\mathbf{j}_e(z) = j_{e\|}(z)\mathbf{b}(z) - en_e\mathbf{v}_E$$
$$+ (p_{e\|} - p_{e\perp})\frac{[\mathbf{b}\times(\mathbf{b}\cdot\nabla)\mathbf{b}]}{B} + \frac{[\mathbf{b}\times\nabla p_{e\perp}]}{B}. \quad (3.6)$$

The electric field is determined from the condition of the longitudinal force equilibrium of electrons (2.3), which in the considered spatially one-dimensional case takes the form

$$E_z = \frac{1}{e\,n_e}\left(-\frac{dp_{e\|}}{dz} + \frac{(p_{e\|} - p_{e\perp})}{B}\frac{dB}{dz}\right). \quad (3.7)$$

In the quasi-neutral plasma with magnetized electrons, the longitudinal electron current is determined from the condition

$$\nabla\cdot\mathbf{j} = 0.$$

In the problem under consideration with fields in the form (3.1), this condition is equivalent to the absence of the z component of the total current density $j_z(z) \equiv 0$. The total current density is determined by the formula

$$\mathbf{j}(z) = \mathbf{j}_i(z) + \mathbf{j}_e(z)$$
$$= \mathbf{j}_i(z) + \mathbf{j}_{e\perp}(z) + j_{e\|}(z)\mathbf{b}(z), \quad (3.8)$$

where the ion current density $\mathbf{j}_i(z)$ is calculated numerically. Substitution of the equality $j_z(z) \equiv 0$ into the z-component of Eq. (3.8) gives an expression for the longitudinal component of the electron current density in terms of the remaining terms

$$j_{e\|}(z) = -\frac{(j_{iz}(z) + j_{e\perp z}(z))}{(\mathbf{b}(z)\cdot\mathbf{e}_z)}$$
$$= -\frac{B(z)}{B_z}(j_{iz}(z) + j_{e\perp z}(z)), \quad (3.9)$$

which leads to the following formulas for the electron current density and total current density

$$\mathbf{j}_e(z) = \mathbf{j}_{e\perp}(z) - \left(j_{iz}(z) + j_{e\perp z}(z)\right)\frac{\mathbf{B}(z)}{B_z},$$
$$\mathbf{j}(z) = \mathbf{j}_i(z) + \mathbf{j}_{e\perp}(z) - \left(j_{iz}(z) + j_{e\perp z}(z)\right)\frac{\mathbf{B}(z)}{B_z}. \quad (3.10)$$

As a result, in the model, the Ampere equation $\nabla \times \mathbf{B} = \mu_0 \mathbf{j}$ is reduced to the following system of two ordinary differential equations of the first order for the self-consistent components of the magnetic field

$$\frac{dB_x(z)}{dz} = \mu_0 j_y(z), \quad \frac{dB_y(z)}{dz} = -\mu_0 j_x(z), \quad (3.11)$$

and the right-hand side may depend on $B_x(z)$ and $B_y(z)$, and also on their derivatives.

Substitution of the expression for the electric field according to formula (3.7) into the second term $e n_e \mathbf{v}_E$ in formula (3.6) and taking into account the form of fields (3.1) makes it possible to obtain an expression for the electron current density in the form

$$\mathbf{j}_e(z) = -j_{iz}\frac{\mathbf{B}}{B_z} - \frac{d}{dz}\left(\frac{\left(p_{e\parallel} - p_{e\perp}\right)}{B^2}[\mathbf{B} \times \mathbf{e}_z]\right). \quad (3.12)$$

Hence it follows that in the case of the isotropic electron pressure $p_{e\parallel} = p_{e\perp} = p_e$ they can only provide a neutralizing longitudinal current

$$\mathbf{j}_e(z) = -j_{iz}(z)\frac{\mathbf{B}(z)}{B_z},$$
$$\mathbf{j}(z) = \mathbf{j}_i(z) - j_{iz}(z)\frac{\mathbf{B}(z)}{B_z}. \quad (3.13)$$

Note that Eq. (3.12) implies the following formulas for the components of the total electron current through CS

$$J_{ex} = \int_{-L}^{L} j_{ex}(z)\,dz = -\int_{-L}^{L} j_{iz}(z)\frac{B_x(z)}{B_z}dz - \left(\frac{\left(p_{e\parallel} - p_{e\perp}\right)}{B^2}B_y\right)(L) + \left(\frac{\left(p_{e\parallel} - p_{e\perp}\right)}{B^2}B_y\right)(-L),$$

$$J_{ey} = \int_{-L}^{L} j_{ey}(z)\,dz = -\int_{-L}^{L} j_{iz}(z)\frac{B_y(z)}{B_z}dz + \left(\frac{\left(p_{e\parallel} - p_{e\perp}\right)}{B^2}B_x\right)(L) - \left(\frac{\left(p_{e\parallel} - p_{e\perp}\right)}{B^2}B_x\right)(-L).$$

In the case of symmetric configurations, the conditions

$$B_x(-z) = -B_x(z), \quad B(-z) = B(z),$$
$$p_{e\parallel}(-L) = p_{e\parallel}(L), \quad p_{e\perp}(-L) = p_{e\perp}(L),$$
$$j_{iz}(z) \equiv 0.$$

From these conditions and the last two formulas, we obtain the equalities

$$J_{ex} = 0, \quad J_{ey} = 2\left(\frac{\left(p_{e\parallel} - p_{e\perp}\right)}{B^2}B_x\right)(L). \quad (3.14)$$

The equalities below follow from the last relation and the first equation in Eq. (3.11) and taking into account the equality $\Delta B = 2B_x(L)$

$$\frac{\Delta B_e}{\Delta B} = \frac{\mu_0 J_{ey}}{2B_x(L)} = \frac{\mu_0}{B^2(L)}\left(p_{e\parallel}(L) - p_{e\perp}(L)\right), \quad (3.15)$$

which means that the relative contribution of electrons to the total current is equal to the ratio of the pressure half-difference $\left(p_{e\parallel}(L) - p_{e\perp}(L)\right)/2$ to the magnetic pressure $B^2(L)/(2\mu_0)$ on the edge of CS. Substitution of the observed characteristic values into this formula shows that within the 1D3V model, in the symmetric case, electrons with the anisotropic pressure can make only a small relative contribution to the total current and to the magnetic field variation upon passing through CS

$$\frac{\Delta B_e}{\Delta B} \sim 0.0003\text{–}0.03. \quad (3.16)$$

In this case, electrons with the anisotropic pressure can significantly change the profile of the current density inside the CS as will be shown below in Section 7.

For the Vlasov equation describing electrons in the drift approximation, the characteristic system is the system of equations of motion of the leading center (see [13, 16, 23–27]). For this system of equations, according to the drift theory, the magnetic moment $\mu(z, v_\perp)$ and total energy (Hamiltonian) $H(z, v_\parallel, v_\perp)$, which are determined by formulas

$$\mu\left(z, v_\perp^2\right) = \frac{v_\perp^2}{2B(z)},$$
$$H\left(z, v_\parallel^2, v_\perp^2\right) = \frac{m_e}{2}\left(v_\parallel^2 + v_\perp^2\right) - e\varphi(z), \quad (3.17)$$

are approximate independent integrals. If a magnetic field of the form Eq. (3.1) has no shear component: $B_y(z) \equiv 0$, the functions $\mu(z, v_\perp)$ and $H(z, v_\parallel, v_\perp)$ are exact integrals, and the general solution of the steady-state Vlasov equation in the drift approximation for electrons has the form of an arbitrary function of these two integrals

$$F_e\left(z, v_\parallel, v_\perp\right) = \Phi\left(\mu\left(z, v_\perp^2\right), H\left(z, v_\parallel^2, v_\perp^2\right)\right), \quad (3.18)$$

where $\Phi(\mu, H)$ is a sufficiently smooth function of two variables. If the shear component of the magnetic field is nonzero: $B_y(z) \neq 0$, then a function of the form Eq. (3.18) is an approximate solution. The simplest option is a special case when electrons in the current sheet and outside it have a Maxwell–Boltzmann distribution in steady-state magnetic and electric fields, i.e., the distribution function of their leading centers can be represented as

$$F_e(z, v_{\|}, v_{\perp}) = \frac{(1+\gamma_0) n_0}{\left(V_{Te0}\sqrt{2\pi}\right)^3} \exp\left(\frac{\varphi(z)}{T_{e0}}\right) \times \exp\left(-\frac{v_{\|}^2}{2V_{Te0}{}^2}\right) \exp\left(-\frac{v_{\perp}^2}{2V_{Te0}{}^2}\left(1+\frac{\gamma_0 B_0}{B(z)}\right)\right), \tag{3.19}$$

where constants $B_0 = B(z_0)$, $n_0 = n(z_0)$, $\gamma_0 = \gamma(z_0) = (p_{e\|}(z_0) - p_{e\perp}(z_0))/p_{e\perp}(z_0)$ are values of the corresponding functions at some point of the sheet z_0. That is, γ_0 is a dimensionless anisotropy parameter ($\gamma_0 = 0$ in the isotropic case), T_{e0} is the electron temperature in this point in eV, and $V_{Te0} = \sqrt{eT_{e0}/m_e}$ is the corresponding electron thermal velocity. The distribution function (3.19) gives the following formulas, which couple the electron density $n_e(z) = n_i(z) = n(z)$ with the scalar potential and magnetic field

$$n(z) = \frac{(1+\gamma_0) n_0 B(z)}{(B(z)+\gamma_0 B_0)} \exp\left(\frac{\varphi(z)}{T_{e0}}\right), \quad \varphi(z) = T_{e\|} \ln\left(\frac{(B(z)+\gamma_0 B_0)}{(1+\gamma_0) B(z)} \frac{n(z)}{n_0}\right), \tag{3.20}$$

and also gives a formula for the longitudinal pressure

$$p_{e\|}(z) = en(z) T_{e0}. \tag{3.21}$$

The first expression implies the constancy of the longitudinal electron temperature in the sheet

$$T_{e\|}(z) = \frac{p_{e\|}(z)}{en_e(z)} = \frac{en(z) T_{e0}}{en(z)} = T_{e0} \equiv \text{const}. \tag{3.22}$$

Therefore, in what follows, the longitudinal temperature is assumed to be constant $T_{e\|} = T_{e0} \equiv \text{const}$.

Also the distribution function (3.19) gives the following formula for the transverse pressure

$$p_{e\perp}(z) = eT_{e\|} n_0 \exp\left(\frac{\varphi(z)}{T_{e\|}}\right)\left(\frac{B(z)}{(B(z)+\gamma_0 B_0)}\right)^2 = \frac{en(z) T_{e\|} B(z)}{(B(z)+\gamma_0 B_0)} = \frac{p_{e\|}(z) B(z)}{(B(z)+\gamma_0 B_0)}. \tag{3.23}$$

It follows from this formula that the transverse electron temperature in the sheet changes with the absolute value of the magnetic field and is determined by the expression

$$T_{e\perp}(z) = \frac{p_{e\perp}(z)}{en(z)} = \frac{T_{e\|} B(z)}{(B(z)+\gamma_0 B_0)}. \tag{3.24}$$

The formula is obtained for the electron pressure difference

$$p_{e\|}(z) - p_{e\perp}(z) = \frac{\gamma_0 B_0 p_{e\|}(z)}{(B(z)+\gamma_0 B_0)} = \frac{eT_{e\|}\gamma_0 B_0 n(z)}{(B(z)+\gamma_0 B_0)}. \tag{3.25}$$

Substitution of this expression into Eq. (3.12) and subsequent substitution of the result into Eq. (3.8) lead to the following expressions for the components of the current density:

$$j_x(z) = j_{ix}(z) - j_{iz}(z)\frac{B_x(z)}{B_z} - eT_{e\|}\gamma_0 B_0 \frac{d}{dz}\left(\frac{B_y(z) n(z)}{(B(z)+\gamma_0 B_0) B^2(z)}\right), \tag{3.26}$$

$$j_y(z) = j_{iy}(z) - j_{iz}(z)\frac{B_y(z)}{B_z} + eT_{e\|}\gamma_0 B_0 \frac{d}{dz}\left(\frac{B_x(z) n(z)}{(B(z)+\gamma_0 B_0) B^2(z)}\right). \tag{3.27}$$

We note that it follows from formulas (3.23) that if the electron pressure is isotropic outside the current sheet $(\gamma_0 = 0)$, then it is also isotropic inside the sheet, the electron temperature is constant: $T_e \equiv \text{const}$, and the electron current density and total current density are determined by formulas (3.13). In this case, formulas (3.19)–(3.25) takes the following form:

$$F_e(z, v_{\|}, v_{\perp}) = \frac{n_0}{\left(V_{Te}\sqrt{2\pi}\right)^3} \exp\left(\frac{\varphi(z)}{T_e}\right) \exp\left(-\frac{v_{\|}^2 + v_{\perp}^2}{2V_{Te}^2}\right), \tag{3.28}$$

$$\varphi(z) = T_e \ln\left(\frac{n(z)}{n_0}\right), \quad p_e(z) = en(z) T_e. \tag{3.29}$$

The work considers symmetric planar TCS configurations, in which the magnetic field has two components: a self-consistent component $B_x(z)$ and a given constant component B_z

$$\mathbf{B}(z) = B_x(z)\mathbf{e}_x + B_z \mathbf{e}_z, \quad \mathbf{j}(z) = j_y(z)\mathbf{e}_y, \quad B_y(z) \equiv 0 \tag{3.30}$$

and the condition of the sheet symmetry is taken into account

$$B_x(-z) \equiv -B_x(z), \quad E_z(-z) \equiv -E_z(z),$$
$$f_\alpha(-z, v_x, v_y, -v_z) \equiv f_\alpha(z, v_x, v_y, v_z), \qquad (3.31)$$
$$\alpha = p, \mathrm{O}, e.$$

As a result of the numerical solution of the steady-state Vlasov equation for ion components at the spatial grid nodes, their distribution functions are calculated $f_\alpha(z, v_x, v_y, v_z)$ on a rectangular uniform grid oriented along the magnetic field in the velocity space. The distribution function for each sort of ions is used to calculate the density $n_\alpha(z)$ and their current density, which has only the y component: $\mathbf{j}_\alpha(z) = j_{\alpha y}(z)\mathbf{e}_y$. They are used to calculate the total ion density and their current density:

$$n_i(z) = \sum_\alpha n_\alpha(z), \quad j_{iy}(z) = \sum_\alpha j_{\alpha y}(z).$$

The electron density was considered equal to the ion density: $n_e(z) \equiv n_i(z) = n(z)$, and its value outside the sheet was selected as the density scale n_0. In the case of isotropic electrons, their current density is zero and, according to Eqs. (3.10) and (3.11), the self-consistent component of the magnetic field $B_x(z)$ was calculated as a result of the numerical solution of the Cauchy problem for the equation

$$\frac{dB_x(z)}{dz} = \mu_0 j_{iy}(z), \qquad (3.32)$$

and the potential of the electric field was calculated using the first formula in Eq. (3.29). In the case of anisotropic electrons their current is determined by the equation

$$j_{ey}(z) = eT_{e\|}\gamma_0 B_0 \frac{d}{dz}\left(\frac{B_x(z)n(z)}{(B(z)+\gamma_0 B_0)B^2(z)}\right), \qquad (3.33)$$

and the nonlinear equation below follows from (3.10)–(3.12)

$$\frac{dB_x(z)}{dz} = \mu_0 \times\left(j_{iy}(z) + eT_{e\|}\gamma_0 B_0 \frac{d}{dz}\left(\frac{B_x(z)n(z)}{(B(z)+\gamma_0 B_0)B^2(z)}\right)\right), \qquad (3.34)$$

for which the Cauchy problem was solved numerically using an iterative process, and the electric field potential was calculated using the second formula in Eq. (3.20).

In all calculations, we used the normal component of the magnetic field of $B_z = 2$ nT and its tangential component outside the sheet $B_{x0} = 20$ nT, the electron temperature was $T_e = 0.5$ keV, half-width of the simulation region was $L = R_\mathrm{E} = 6400$ km, the spatial grid step was $\Delta z = R_\mathrm{E}/640 = 10$ km, and the grid step in the velocity space for each sort of ions ($\alpha = p$, O^+) was 1/16 of their thermal velocity in fluxes $\Delta v_\alpha = V_{T\alpha}/16$.

4. RESULTS OF SIMULATION OF TCS CONSISTING ONLY OF PROTONS

We consider symmetric TCS configurations with the isotropic electron pressure, which are formed by proton fluxes, in order to illustrate the dependence of the configurations on the flux parameter $\delta_p = V_{Dp}/V_{Tp}$ and its temperature.

Figure 2 demonstrates the dependence of the profiles of the self-consistent component $B_x(z)$ of the magnetic field, proton current density components $j_{py}(z)$ and density $n_p(z)$ on the flux parameter δ_p at the flux temperature $T_p = 4$ keV. We considered eight values $\delta_p = 0.25$, 0.5, 1, 1.5, 2.5, 4, 5, and 6.25. Plots for $\delta_p = 0.25$ are shown with dark blue lines, for $\delta_p =$ 0.5—violet lines, for $\delta_p = 1$—green lines, for $\delta_p =$ 1.5—brown lines, for $\delta_p = 2.5$—blue lines, for $\delta_p =$ 4—red lines, for $\delta_p = 5$—black lines, and $\delta_p = 6.25$—light blue lines.

Figure 2 shows that profiles of the tangential component of the magnetic field $B_x(z)$ and proton current density components $j_{py}(z)$ are relatively weakly dependent on the parameter δ_p. For a fixed variation of the tangential component of the magnetic field when passing through CS $\Delta B_x = B_x(L) - B_x(-L) = 2B_{x0}$, the density profiles decrease several times slower than $1/\delta_p^2$ when δ_p increases. That is, the counter currents with the high longitudinal velocity and low concentration can form TCS. In the satellite measurements of the TCS of the near-Earth tail, the density values usually do not exceed 1 cm^{-3}. Therefore, variants with small values of the parameter $\delta_p = 0.25$, 0.5—dark blue and violet lines in Fig. 2c, for which this value is exceeded, are not implemented in practice, and variants with $\delta_p \geq 1$ are quite possible.

We note that the current density and density profiles at the center of the sheet have a characteristic "bifurcation" (also called splitting), which increases with the increase of δ_p. As shown in [6, 31, 32], bifurcation is due to the dynamics of quasi-captured protons in the central part of the sheet. The bifurcation intensifies with the increase in the fraction of such protons. Reflection of this fine effect in the results of numerical simulations demonstrates the high quality of the numerical model.

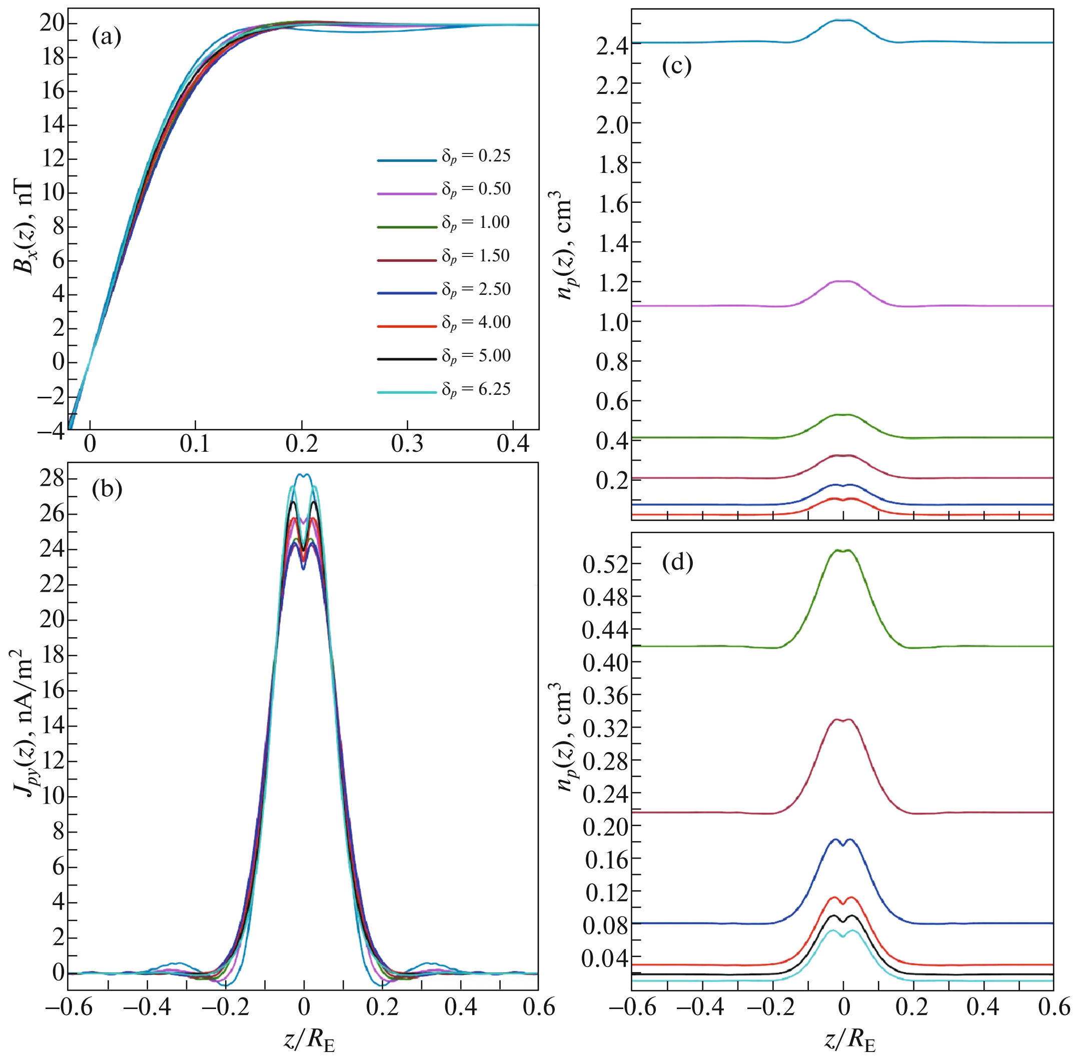

Fig. 2. Profiles of TCSs formed by proton fluxes with $T_p = 4$ keV for eight parameter values $\delta_p = V_{Dp}/V_{Tp}$: (a) magnetic field component $B_x(z)$ in nT (due to the symmetry $B_x(-z) \equiv -B_x(z)$, the right-hand part at $z/R_E \geq -0.2$ is shown); (b) proton current density component $j_{py}(z)$ in nA/m^2; and (c) and (d) profiles of the density $n_p(z)$ in cm^{-3}.

We also note that the ratio of the maximum density value to its value at the edge of the sheet $n_{max}/n(L)$ is somewhat smaller than the parameter δ_p, i.e., $n_{max}/n(L) \approx \delta_p$. This information can be useful for analyzing data obtained using spacecraft.

To demonstrate the role of the flux temperature T_p, Fig. 3 shows the profiles of the TCS configurations for two values of the temperature of the incident fluxes $T_p = 4$ keV (brown lines; in Fig. 2, it is shown with the same color) and $T_p = 10$ keV (blue lines) at the same value of the flux parameter $\delta_p = 1.5$. It is seen from the figure that the CS becomes thicker with increasing temperature, while the maximum value of the current density in the center of the sheet and the density values decrease.

Violet lines in Fig. 3 show the TCS configuration at $T_p = 10$ keV and $\delta_p = 0.5$. The configuration with the same value $\delta_p = 0.5$ at the flux temperature $T_p = 4$ keV is shown in Fig. 2 also with violet lines. The comparison of the corresponding density profiles shows that for profiles with the same δ_p value, the ratio of density values at the CS edges is approximately equal to the inverse ratio of flux temperatures

$$T_{p1} n_p(L)\big|_{T_{p1}} \approx T_{p2}\, n_p(L)\big|_{T_{p2}}. \tag{4.1}$$

To elucidate the effect of the background proton population, the following calculations were carried out. The equilibrium configurations were obtained for the two flux options shown in Fig. 3, in which, in addition to counter fluxes, there is a background proton

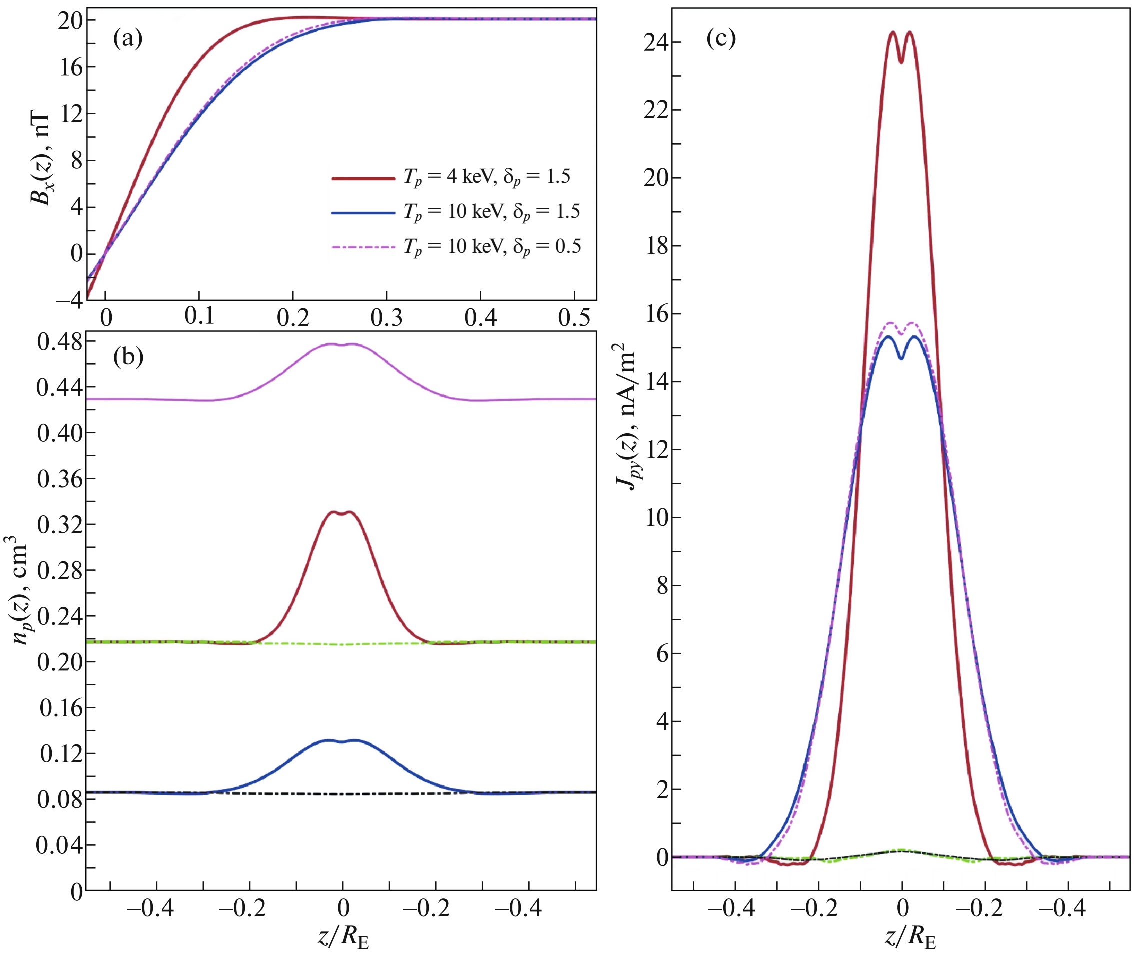

Fig. 3. Profiles of TCSs formed by proton fluxes at $\delta_p = 1.5$ for two values of the flux temperature: $T_p = 4$ keV—brown lines and $T_p = 10$ keV—blue lines: (a) magnetic field component $B_x(z)$ in nT; (b) density $n_p(z)$ in cm^{-3}; and (c) proton current density component $j_{py}(z)$ in nA/m^2 (c). The green lines show the density and current density of the background protons for the first configuration, and the black lines for the second configuration.

population with the temperature of $T_p = 4$ keV, for which in formula (3.5) the flux velocity is $V_{Dp} = 0$, and the density at CS edges coincides with the density of the particle population, which supports the current. The contribution of the background population for the first option with the flux temperature $T_p = 4$ keV is shown with green lines, and that for the second option with the flux temperature $T_p = 10$ keV is shown with black lines. The total values of the current density and the magnetic field, which is determined by the current density, changed slightly, so we do not give them.

Simulation showed that the density profile of the background population is close to constant. In the center of the sheet in the region of the increasing density of the "current-carrying" population, the background density has a barely noticeable decrease, and the background current density also appears, which is more than 100 times less than the current density of the "current-carrying" population. In this case, the total current through the sheet from the background population is zero, i.e., it gives a zero contribution to the magnetic field difference across CS. According to the first formula in Eq. (3.29), the appearance of the background population reduces the scalar potential and the electric field, since the ratio $n(z)/n(L)$ (it is equal to unity at CS edges) decreases in the center of the sheet. But this change has almost no effect on the motion of hot protons of the "current-carrying" population.

Thus, the expected conclusion is that the effect of the background population on the current density and magnetic field in TCS is very small, and it can be neglected.

Figures 4 and 5 show the dependence of the distribution function at the center of the CS on the longitudinal flux velocity, which is conveniently represented as a dependence on the parameter δ_p. In the model, at each node of the spatial grid, to calculate the proton

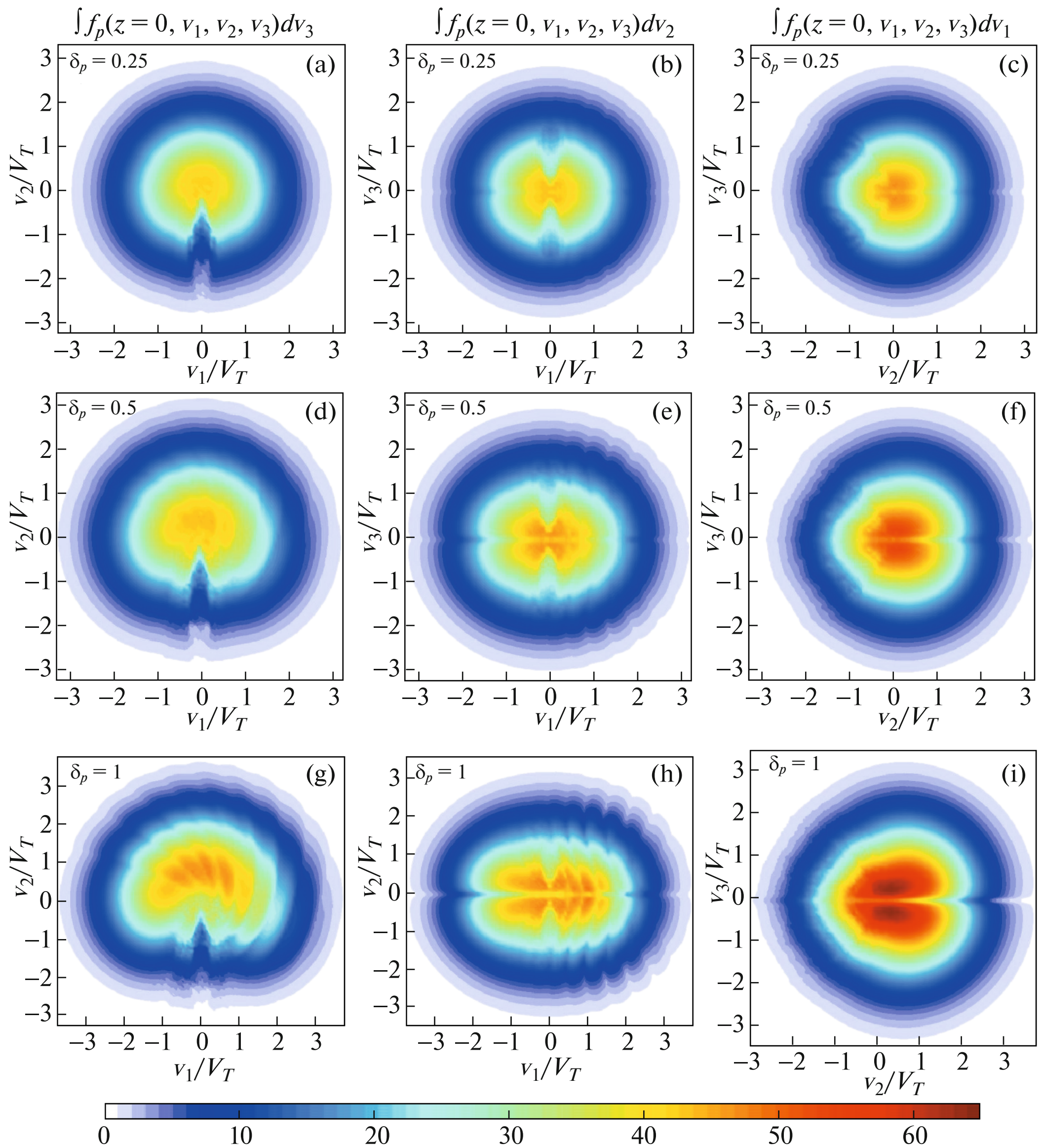

Fig. 4. Plots of dimensionless functions (4.3)–(4.5) for protons at the point $z = 0$ in the CS center for three values of the parameter $\delta_p = 0.25$, 0.5, and 1. Plots of the function $F_{p1,2}(z = 0, v_1/V_{Tp}, v_2/V_{Tp})$ are shown in panels (a), (d), and (g), respectively. Plots of the function $F_{p1,3}(z = 0, v_1/V_{Tp}, v_3/V_{Tp})$ are shown in panels (b), (e), and (h). Plots of the function $F_{p2,3}(z = 0, v_2/V_{Tp}, v_3/V_{Tp})$ are shown in panels (c), (f), and (i).

distribution function in the velocity space, a Cartesian coordinate system associated with the magnetic field is used, in which the basis vectors and velocity components are determined by the formulas

$$\mathbf{h}_3(z) = \mathbf{b}(z), \quad \mathbf{h}_1(z) = \frac{B_z\mathbf{e}_x - B_x(z)\mathbf{e}_z}{B(z)},$$
$$\mathbf{h}_2(z) = [\mathbf{b}(z) \times \mathbf{h}_1(z)] \equiv \mathbf{e}_y, \tag{4.2}$$
$$v_k(z) = (\mathbf{v} \cdot \mathbf{h}_k(z)), \quad k = 1, 2, 3.$$

That is, the component $v_3(z) = v_{\|}(z)$ is the longitudinal velocity along the magnetic field, and the $v_1(z)$ and $v_2(z)$ components are orthogonal to the magnetic field. In this case, in the case under consideration, the magnetic field is of the form (4.1) $v_2(z) = v_y$. The equalities $v_1(0) = v_x$ and $v_3(0) = v_z$ hold in the CS center at $z = 0$.

To display the distribution functions $f_\alpha(z, v_1, v_2, v_3)$ of each sort of ions $\alpha = p, \mathrm{O}^+$, it is convenient to show the plots of the following dimensionless functions of dimensionless velocities, which are obtained as a result of its integration over one of the velocity

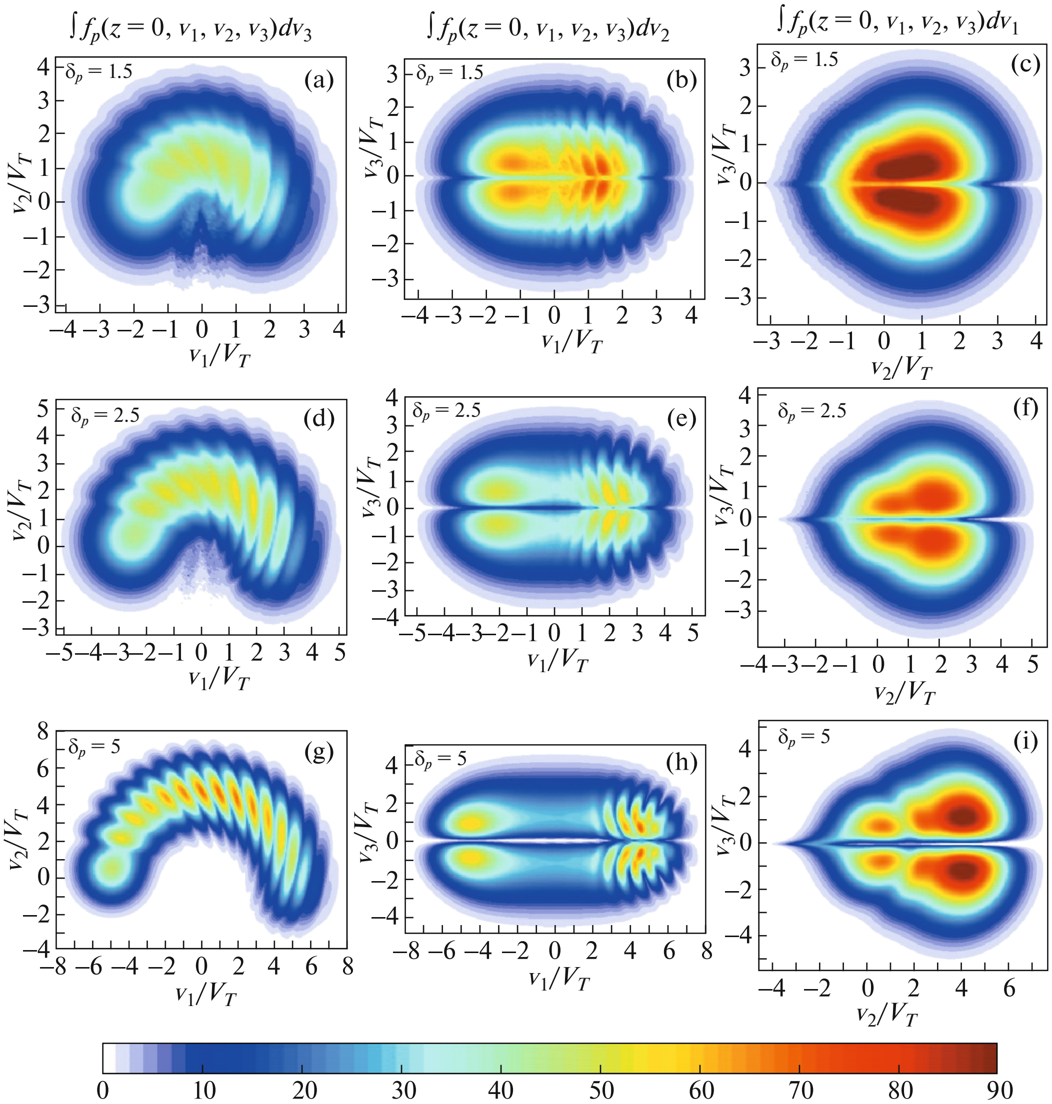

Fig. 5. Same plots as in Fig. 4 for $\delta_p = 1.5$, 2.5, and 5.

components in the coordinate system associated with the magnetic field

$$F_{\alpha 1,2}\left(z, \frac{v_1}{V_{T\alpha}}, \frac{v_2}{V_{T\alpha}}\right) = \frac{V_{T\alpha}^2}{\tilde{n}_{\alpha 0}} \int_{-\infty}^{+\infty} f_\alpha(z, v_1, v_2, v_3)\, dv_3, \quad (4.3)$$

$$F_{\alpha 1,3}\left(z, \frac{v_1}{V_{T\alpha}}, \frac{v_3}{V_{T\alpha}}\right) = \frac{V_{T\alpha}^2}{\tilde{n}_{\alpha 0}} \int_{-\infty}^{+\infty} f_\alpha(z, v_1, v_2, v_3)\, dv_2, \quad (4.4)$$

$$F_{\alpha 2,3}\left(z, \frac{v_2}{V_{T\alpha}}, \frac{v_3}{V_{T\alpha}}\right) = \frac{V_{T\alpha}^2}{\tilde{n}_{\alpha 0}} \int_{-\infty}^{+\infty} f_\alpha(z, v_1, v_2, v_3)\, dv_1, \quad (4.5)$$

where $\tilde{n}_{\alpha 0}$ is the dimensional density scale.

Figure 4 shows the plots of these functions for protons in the point $z = 0$ in the CS center for three parameter values $\delta_p = 0.25$, 0.5, and 1. Plots of the function $F_{p1,2}(z = 0, v_1/V_{Tp}, v_2/V_{Tp})$ are shown in the left-hand column: for $\delta_p = 0.25$ in Fig. 4a, for $\delta_p = 0.5$ in Fig. 4d, and for $\delta_p = 1$ in Fig. 4g. Plots of the function $F_{p1,3}(z = 0, v_1/V_{Tp}, v_3/V_{Tp})$ are shown in the central column: for $\delta_p = 0.25$ in Fig. 4b, for $\delta_p = 0.5$ in Fig. 4e, and for $\delta_p = 1$ in Fig. 4h). Plots the function $F_{p2,3}(z = 0, v_2/V_{Tp}, v_3/V_{Tp})$ are shown in the right-hand column: for $\delta_p = 0.25$ in Fig. 4c, for $\delta_p = 0.5$ in Fig. 4f, and for $\delta_p = 1$ in Fig. 4i.

Figure 5 shows analogous plots for three other parameter values $\delta_p = 1.5$, 2.5, and 5. Plots of the function $F_{p1,2}(z = 0, v_1/V_{Tp}, v_2/V_{Tp})$ are shown in the left-hand column: for $\delta_p = 1.5$ in Fig. 5a, for $\delta_p = 2.5$ in Fig. 5d, and for $\delta_p = 5$ in Fig. 5g. Plots of the function $F_{p1,3}(z = 0, v_1/V_{Tp}, v_3/V_{Tp})$ are shown in the central

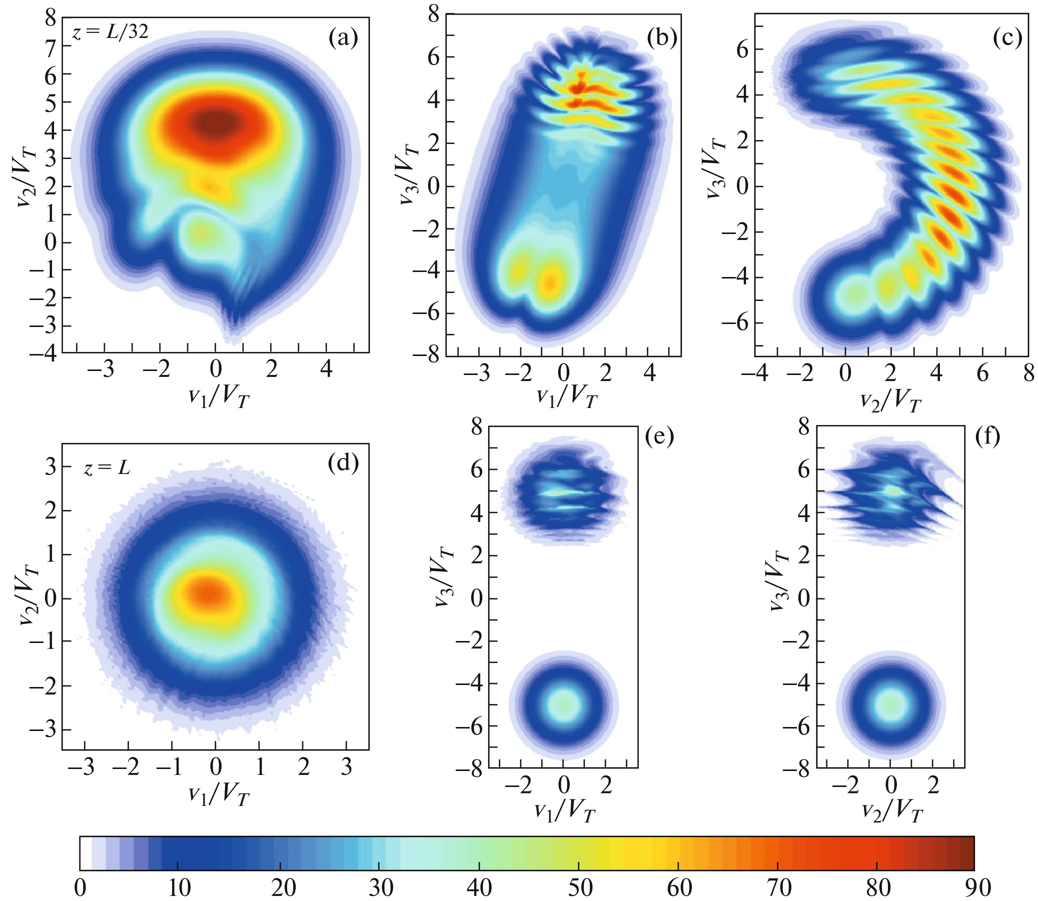

Fig. 6. Plots of dimensionless functions (4.3)–(4.5) for $\delta_p = 5$ in two points: in the point $z = R_E/32$ in panels (a), (b) and (c), and in the point $z = R_E$ in panels (d), (e), and (f).

column: for $\delta_p = 1.5$ in Fig. 5b, for $\delta_p = 2.5$ in Fig. 5e and for $\delta_p = 5$ in Fig. 5h. Plots of the function $F_{p2,3}(z = 0, v_2/V_{Tp}, v_3/V_{Tp})$ are shown in the right-hand column: for $\delta_p = 1.5$ in Fig. 5c, for $\delta_p = 2.5$ in Fig. 5f, and for $\delta_p = 5$ in Fig. 5i.

These figures show the distribution function of two opposite fluxes in the CS center, which at the increase in the parameter δ_p (i.e., with an increase in the longitudinal hydrodynamic flux velocity V_{Dp}) are more and more divided. Figures 4a, 4d, 4g, 5a, 5d, 5g in the left-hand column in Figs. 4 and 5 demonstrate that the plot of the distribution function on the orthogonal velocity components $F_{p1,2}(z = 0, v_1/V_{Tp}, v_2/V_{Tp})$ first take the "mushroom" form ($\delta_p = 1, 1.5$), and them transforms into the well-known shape of a horseshoe, while the radius of the "central arc" of the horseshoe is approximately equal to the parameter δ_p.

Figures 4b, 4e, 4h and 5b, 5e, 5h in the central column and Figs. 4b, 4e, 4i, 5b, 5f, 5i in the right-hand column for the distribution functions $F_{p1,3}(z = 0, v_1/V_{Tp}, v_3/V_{Tp})$ and $F_{p2,3}(z = 0, v_2/V_{Tp}, v_3/V_{Tp})$ demonstrate the decrease in the region of overlap of counter fluxes in the velocity space with the increase in the parameter δ_p.

Figure 6 for the variant with $\delta_p = 5$ shows the plots of the distribution functions (4.3)–(4.5) for protons in two points: in the point $z = R_E/32$ near the CS center and in the point $z = R_E$ at the edge of the simulation region. The plot of $F_{p1,2}(z, v_1/V_{Tp}, v_2/V_{Tp})$ in the point $z = R_E/32$ is shown in Fig. 6a and in the point $z = R_E$ in Fig. 6d, the plot of $F_{p1,3}(z, v_1/V_{Tp}, v_3/V_{Tp})$ in the point $z = R_E/32$ is shown in Fig. 6b, and in the point $z = R_E$ in Fig. 6e, the plot of $F_{p2,3}(z, v_2/V_{Tp}, v_3/V_{Tp})$ in the point $z = R_E/32$ in Fig. 6c and in the point $z = R_E$ in Fig. 6f.

Figure 7 for eight parameters $\delta_p = 0.25, 0.5, 1, 1.5, 2.5, 4, 5$, and 6.25 and the point $z = 0$ in the CS center shows the plots of the dimensionless longitudinal dis-

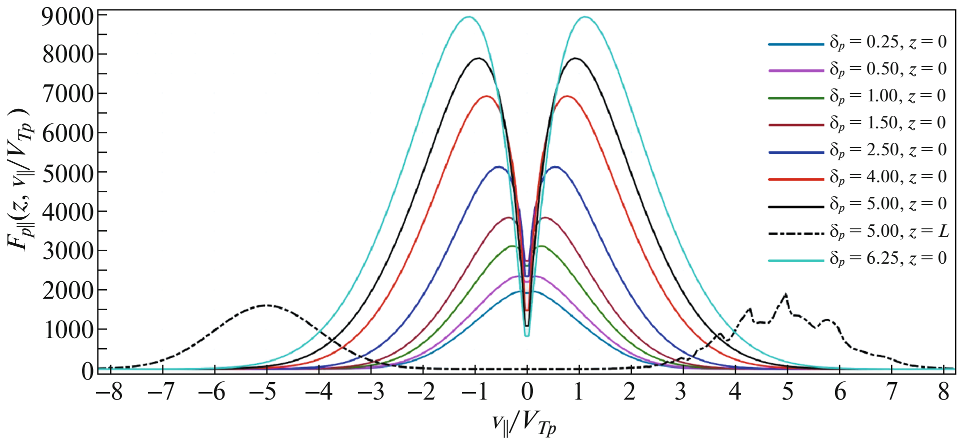

Fig. 7. Longitudinal distribution function $F_{p\|}\left(z, v_\|/V_{Tp}\right)$ in the CS center in the point $z = 0$ for eight parameter values $\delta_p = 0.25$, 0.5, 1, 1.5, 2.5, 4, 5, 6.25, and also on the edge of the simulation region in the point $z = R_{\rm E}$ for the parameter $\delta_p = 5$ (black dash-dotted line).

tribution function for protons $F_{p\|}\left(z, v_\|/V_{Tp}\right)$, which is determined by the formula

$$F_{\alpha\|}\left(z, \frac{v_\|}{V_{T\alpha}}\right) = \frac{V_{T\alpha}}{\tilde{n}_{\alpha 0}} \int\limits_{-\infty}^{+\infty}\int\limits_{-\infty}^{+\infty} f_\alpha\left(z, v_1, v_2, v_\|\right) dv_1 dv_2, \qquad (4.6)$$

where $\tilde{n}_{\alpha 0}$ is the dimensional density scale, and, in accord with notations in Eq. (4.2), $v_\| = v_3$. In addition, the black dash-dotted line in Fig. 7 shows this function at the edge of the simulation region in the point $z = R_{\rm E}$ for the parameter $\delta_p = 5$. It can be seen in Fig. 7 that at small values of the parameter δ_p the counter fluxes in the CS center overlap, and with the increase in this parameter they are divided more and more. In this case, the longitudinal velocities of the oncoming fluxes in the center of the sheet are several times less than their longitudinal velocity V_{Dp} at the edges of the sheet.

The comparison of the plot in Fig. 5g with the plot in Fig. 6c shows that the plot of the function $F_{p2,3}\left(z = R_{\rm E}/32, v_2/V_{Tp}, v_3/V_{Tp}\right)$ in Fig. 6c is very similar to the plot of the function $F_{p1,2}(z = 0, v_1/V_{Tp}, v_3/V_{Tp})$ in Fig. 5g. These figures show a very close horseshoe-shaped structure and a conditional transition of the velocity components $v_3 \to v_1$, $v_1 \to v_3$ when approaching the central point sheet $z = 0$, and also the corresponding mutual transition of functions

$$F_{p2,3}\left(z, v_2/V_{Tp}, v_3/V_{Tp}\right)$$
$$\leftrightarrow F_{p1,2}\left(0, v_1/V_{Tp}, v_2/V_{Tp}\right) \quad \text{for} \quad z \to 0.$$

This transition is caused by a sharp turn of the magnetic field line when approaching the central point of the sheet $z = 0$.

It can be seen also that the plot of the function $F_{p1,3}\left(z = R_{\rm E}/32, v_1/V_{Tp}, v_3/V_{Tp}\right)$ in Fig. 6b is very similar to the rotated plot of the function $F_{p1,3}(z = 0, v_1/V_{Tp}, v_3/V_{Tp})$ in Fig. 5h. The calculation results show the following pattern of the change in the proton distribution function from the edges of the simulation region to the center of the sheet. At the edge of the CS, there are two fluxes: an incident flux from the source on the side of the investigated CS, and also a counter flux. The counter flux consists of reflected phase trajectories from the source on the side of CS in question, and also of trajectories from the source passing through the sheet from the opposite side of CS. The incident flux for the parameter $\delta_p = 5$ in Fig. 6d and 6f is shown by the lower regular circles with the Maxwellian distribution, and in Fig. 7 it is shown on the left-hand side of the plot of the longitudinal distribution function $F_{p\|}\left(z = R_E, v_\|/V_{Tp}\right)$ with a maximum in the point $v_\|/V_{Tp} = -5$ (this plot is indicated by a black dash-dotted line). The counter flux in Figs. 6e and 6f is shown by the upper spot, while in Fig. 7, it is presented by the right-hand side of the plot of the longitudinal distribution function $F_{p\|}\left(z = R_{\rm E}, v_\|/V_{Tp}\right)$ with a maximum in the point $v_\|/V_{Tp} \approx 5$.

When approaching the center of the sheet, the fluxes converge and mix. A pattern similar to that shown in Figs. 6a–6c is established at about a distance $z = 0.1R_{\rm E}$. At the same time, on the central panel, the structure rotates more and more from the vertical direction to the horizontal direction.

Ideally symmetric cases do not occur in CS observed on spacecraft, but nearly symmetric CS are encountered. Due to the discrete time of checking the devices, it is not always possible to obtain the distribu-

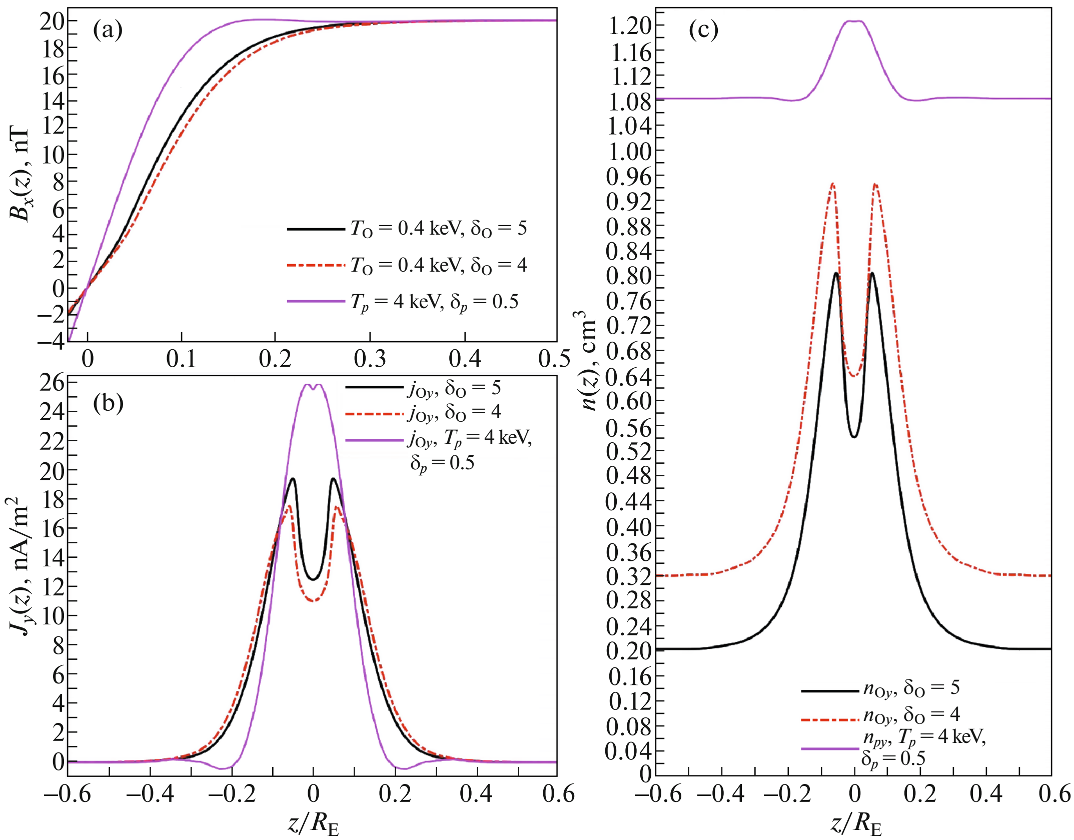

Fig. 8. Profiles of TCSs formed by oxygen ion fluxes at T_O = 0.4 keV and two values δ_O = 4—red lines, and 5—black lines: (a) magnetic field component $B_x(z)$ in nT; (b) proton current density component $j_{Oy}(z)$ in nA/m^2; and (c) density $n_O(z)$ in cm^{-3}. For comparison, violet lines show proton TCS profiles at δ_p= 0.5 and T_p = 4 keV.

tion function exactly in the center of the CS. Therefore, the measurement data for a nearly symmetric CS near its center shows a picture similar to Figs. 6a–6c.

To analyze experimental data for the current sheets, it is necessary to construct the plots of distribution functions (4.3)–(4.6) similar to those shown in Figs. 4–7 at points in the center of CS and on its edges. That is, the velocity components should be calculated not in the same coordinate system for the entire CS, but in the local coordinate system determined by formulas (4.2) related to the magnetic field. From these plots it is possible to draw conclusions about the parameters of the incident fluxes and their behavior in CS.

5. RESULTS OF SIMULATION OF TCS CONSISTING ONLY OF OXYGEN IONS

We consider symmetric TCS configurations formed by oxygen ion fluxes, when proton fluxes are absent, i.e., protons are a background, the effect of which we neglect. The electron pressure is also considered isotropic, i.e., they do not contribute to the current density.

Figure 8 shows two current sheet configurations with the ion temperature T_O = 0.4 keV. The configuration with the flux parameter δ_O = 4 is shown with red lines, and the configuration with δ_O = 5 is shown with black lines. The values of the longitudinal velocity $V_{DO} \approx 200$ km/s and $V_{DO} \approx 250$ km/s correspond to these δ_O values. All other parameters of the model are the same as indicated in the previous section. For comparison violet line shows the configuration formed by proton fluxes with the close value $V_{Dp} \approx$ 310 km/s, for which $T_p = 4$ keV and δ_p = 0.5. In Fig. 2, it is also shown with the violet line.

The comparison of Figs. 2 and 8 shows that the CS formed by oxygen ions fluxes has the following differences from the CS supported by proton fluxes: (1) CS on oxygen ions is about 1.5 times wider; (2) the dip in the center of the sheet (splitting or bifurcation) in the current density and density profiles is an order of magnitude stronger. The density values at the edge of the sheet with the same flux parameter $\delta_O = \delta_p$ correspond to the estimate (4.1), i.e.,

$$T_O n_O(L) \approx T_p n_p(L),$$

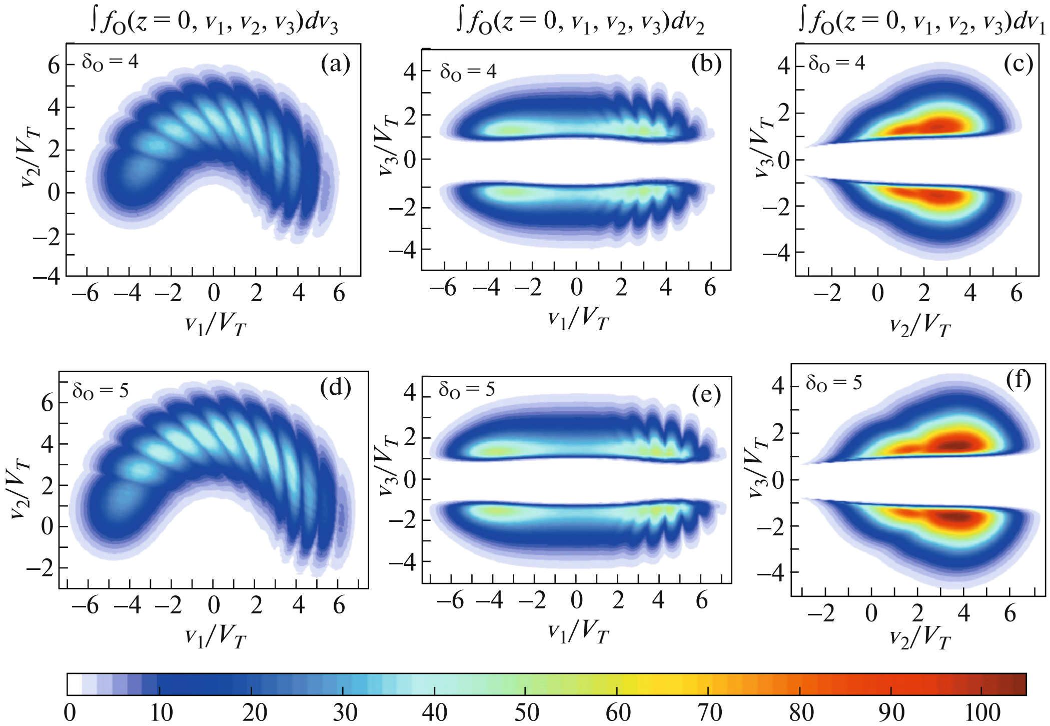

Fig. 9. Plots of dimensionless functions (4.3)–(4.5) for oxygen ions in the CS center for two values of the parameter $\delta_O = 4$, 5. Plots of the function $F_{O1,2}(z = 0, v_1/V_{TO}, v_2/V_{TO})$ are shown in panels (a) and (d), respectively. Plots of the function $F_{O1,3}(z = 0, v_1/V_{TO}, v_3/V_{TO})$ are shown in panels (b) and (e). Plots of the function $F_{O2,3}(z = 0, v_2/V_{TO}, v_3/V_{TO})$ are shown in panels (c) and (f).

and its maximum values near the center of the sheet are less than 1 cm $^{-3}$, i.e., are in agreement with the experimental data.

Figure 9, similarly to Figs. 4 and 5, shows the plots of the distribution functions (4.3)–(4.5) for oxygen ions in the point $z = 0$ in the CS center for two parameters $\delta_O = 4$, 5. Plots of the function $F_{O1,2}(z = 0, v_1/V_{TO}, v_2/V_{TO})$ are shown for $\delta_O = 4$ in Fig. 9a and for $\delta_O = 5$ in Fig. 9d. Plots of the function $F_{O1,3}(z = 0, v_1/V_{TO}, v_3/V_{TO})$ are shown for $\delta_O = 4$ in Fig. 9b and for $\delta_O = 5$ in Fig. 9e. Plots of the function $F_{O2,3}(z = 0, v_2/V_{TO}, v_3/V_{TO})$ are shown for $\delta_O = 4$ in Fig. 9c and for $\delta_O = 5$ in Fig. 9f.

Figure 10, similarly to Fig. 6, shows the plots of the distribution functions (4.3)–(4.5) for oxygen ions for the variant with $\delta_O = 5$ in two points: in the point $z = R_E/32$ near the CS center and in the point $z = R_E$ at the edge of the simulation region. The plot of $F_{O1,2}(z, v_1/V_{TO}, v_2/V_{TO})$ in the point $z = R_E/32$ is shown in Fig. 10a and in the point $z = R_E$ in Fig. 10d, the plot of $F_{O1,3}(z, v_1/V_{TO}, v_3/V_{TO})$ in the point $z = R_E/32$ is shown in Fig. 10b and in the point $z = R_E$ in Fig. 10e, the plot of $F_{O2,3}(z, v_2/V_{TO}, v_3/V_{TO})$ in the point $z = R_E/32$ is shown in Fig. 10c and in the point $z = R_E$ in Fig. 10f.

Figure 11, analogous to Fig. 7, shows the plots of the longitudinal distribution function of oxygen ions $F_{O\|}(z, v_\|/V_{TO})$ (which is determined by formula (4.6)) in the point $z = 0$ in the CS center for two values of the flux parameter $\delta_O = V_{DO}/V_{TO} = 4$, 5. In addition, the black dash-dotted line shows this function at the edge of the simulation region in the point $z = R_E$ for the parameter $\delta_O = 5$.

The comparison of Figs. 9d and 5g show that the horseshoe shapes in these figures are very close at the same parameter $\delta_O = \delta_p = 5$. The comparison of Figs. 9e and 5h and comparison of Figs. 9f and 5i, and also comparison of Figs. 11 and Fig. 7 shows that in the CS center, the counter oxygen ion fluxes have a higher longitudinal velocity and in the space of velocities, are separated by the longitudinal velocity (empty band $\{|v_3/V_{TO}| < 0.6\}$ in Figs. 9e and 9f), and also have a sharp inner boundary and a smaller size along the longitudinal velocity, while for hotter protons these fluxes in the velocity space are not completely separated, their inner boundary is smoother, and the tail of the flux is longer. The comparison of Figs. 10b and 6b

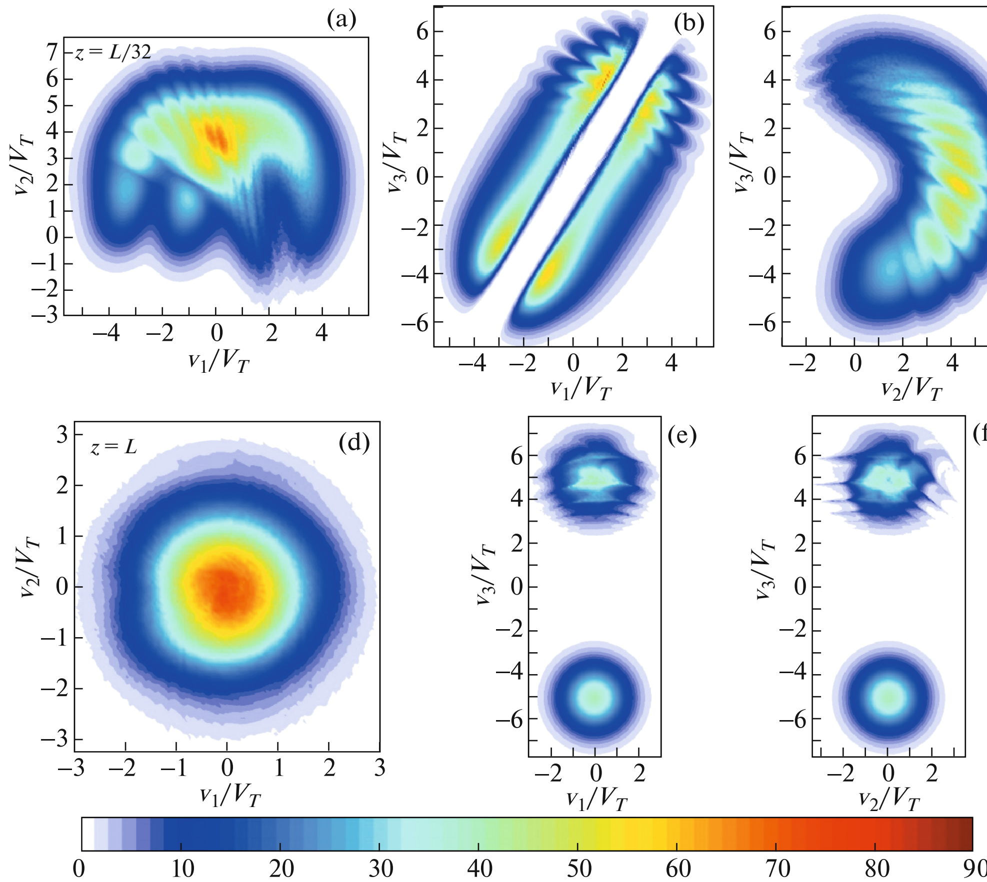

Fig. 10. Plots of dimensionless functions (4.3)–(4.5) for oxygen ions at the parameter $\delta_O = 5$ in two points: in the point $z = R_E/32$ (a–c), and in the point $z = R_E$ (d–f).

shows that in Fig. 10b, the direction of the characteristic structure is closer to the horizontal one. The comparison of Figs. 10c and 6c and Figs. 10a and 6a shows a more pronounced onset of the mutual transition process

$$v_3 \to v_1, \quad v_1 \to v_3,$$
$$F_{O2,3}(z, v_2/V_{TO}, v_3/V_{TO}) \leftrightarrow F_{O1,2}(0, v_1/V_{TO}, v_2/V_{TO})$$
$$\text{at} \quad z \to 0$$

in Fig. 10. This is due to the fact that the CS on oxygen ions is wider (as noted above when comparing Figs. 2 and 8), and this transition begins at a larger distance from the center of the sheet. For CS consisting only of protons, this transition is more pronounced in the points even closer to the CS center.

Thus, one can conclude from the simulation results that under disturbed conditions CS in the near-Earth magnetotail can be formed by oxygen ion fluxes in the absence of proton fluxes. This CS has a number of differences from the TCS formed by the proton fluxes, which is interesting to check from the experimental data of CS intersections under perturbed conditions.

6. TCS CONSISTING OF A MIXTURE OF PROTONS AND OXYGEN IONS

From the point of view of a possible scenario of the formation of TCS of the near-Earth tail of the magnetosphere under disturbed conditions, it is quite possible that there are both oxygen ion fluxes and protons fluxes with comparable longitudinal hydrodynamic velocities $V_{DO} \sim V_{Dp}$ and densities on the edges of the sheet $n_O(L) \sim n_p(L)$. To simulate this situation, a steady-state TCS configuration was obtained with the parameters of the oxygen ion and proton fluxes, for which the TCS configurations were calculated separately (they are shown in Figs. 2 and 8). The oxygen ion flux parameters were $T_O = 0.4$ keV and $\delta_O = 5$, i.e., $V_{DO} \approx 250$ km/s. The parameters of the proton flux were $T_p = 4$ keV, $\delta_p = 0.5$, i.e., $V_{Dp} \approx 310$ km/s. The densities on the edges of the sheet considered to be the same: $n_O(L) = n_p(L)$. The electron pressure was still considered isotropic, i.e., their current is zero. The calculation results are shown in Fig. 12. For comparison, black lines show the profiles for TCS consist-

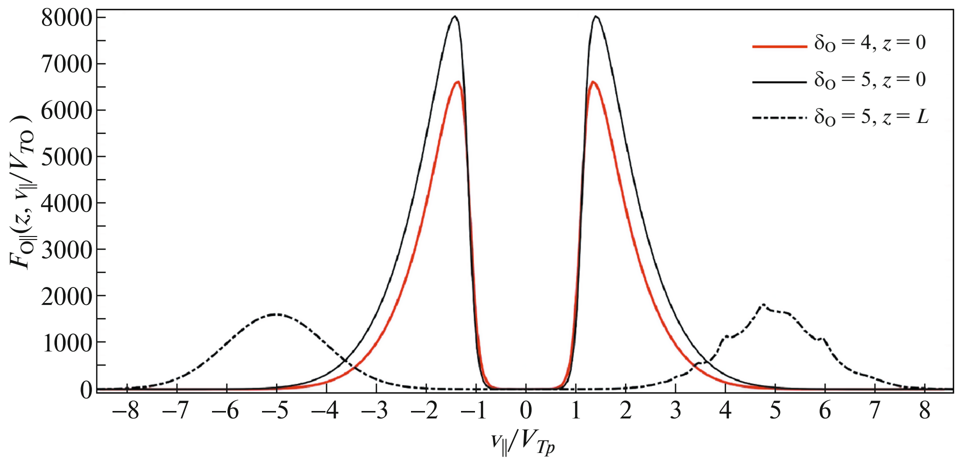

Fig. 11. Longitudinal distribution function $F_{O\parallel}(z, v_\parallel/V_{TO})$ of oxygen ions in the point $z = 0$ in the CS center for two values of the flux parameter $\delta_O = 4, 5$ (solid red and black lines, respectively), and also this function at the edge of the simulation region in the point $z = R_E$ for the parameter $\delta_O = 5$ (black dash-dotted line).

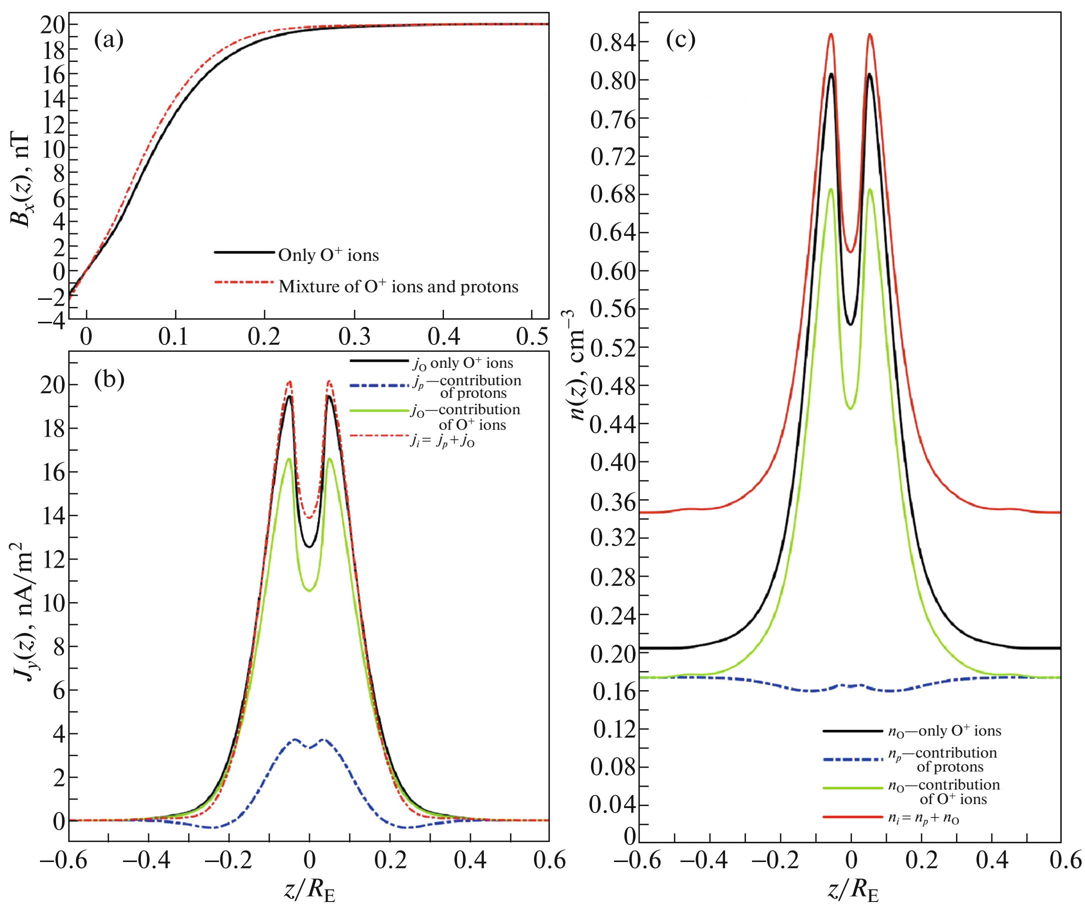

Fig. 12. Red lines show profiles of the TCS formed by oxygen ion fluxes with parameters $T_O = 0.4$ keV, $\delta_O = 5$ and proton fluxes with parameters $T_p = 4$ keV, $\delta_p = 0.5$: (a) magnetic field component $B_x(z)$ in nT; (b) current density component $j_y(z) = j_{Oy}(z) + j_{py}(z)$ in nA/m^2; and (c) ion density $n_i(z) = n_O(z) + n_p(z)$ in cm^{-3}. Green lines in panels (b) and (c) show the contribution of oxygen ions, and blue lines show the contribution of protons. For comparison, black lines show profiles of the TCS formed only by oxygen ion fluxes.

ing only of oxygen ions, which are shown in Fig. 8 also with black lines.

One can see in Fig. 12 that the main contribution to the total current through CS comes from oxygen ions. Their contribution is shown with green lines and the contribution of protons is shown with blue lines.

The onset of the population of "current-carrying" protons makes the CS thinner, but the profiles of the magnetic field and total ion current (shown by red lines) differ relatively little from the corresponding TCS profiles on oxygen ions alone (shown by black lines). In this case, the proton current is negative at the edges of the sheet and compensates for the positive oxygen ion current, which leads to a slight narrowing of CS. Also, the onset of the population of "current-carrying" protons reduces the scalar potential and the electric field, since the $n(z)/n(L)$ ratio appearing in formula (3.30) for the potential in the center of the sheet decreases. But this change has little effect on the motion of oxygen ions forming the CS with a sufficiently high longitudinal velocity, and also on the motion of hot protons.

We note that the shape of the density proton profile differs significantly from that of the profile for the TCS consisting only of protons with the same flux parameters, which is shown by the violet line in Figs. 2 and 3. In the central region of the TCS, where the positive oxygen ion current is present, the proton density profile has a wide decrease, in the center of which there is a slight increase with an even smaller decrease in the center. In this case, the total ion density (red line in Fig. 12c) lies within the limits which are observed in the experimental data.

These changes show that in the magnetic field of the thicker TCS, which is mainly created by the oxygen ion current, the motion of the protons changes in comparison with their motion in the narrower TCS, formed only by their currents.

In addition, similar TCS configurations were obtained with higher longitudinal velocity of protons V_{Dp}, in which the parameter $\delta_p = V_{Dp}/V_{Tp}$ was 1 and 1.5. In these configurations, there is no longer any decrease in the proton density in the center of the sheet, and the relative contribution of protons to the total current increases. From the simulation results, it can be concluded that the scenario of the TCS formation by oxygen ion fluxes and proton fluxes with comparable values of the longitudinal hydrodynamic velocity under disturbed conditions in the near-Earth tail of the magnetosphere is quite possible.

7. EFFECT OF ANISOTROPIC ELECTRONS

To show the differences in the current density profile of anisotropic electrons between the TCS formed only by proton fluxes and the TCS formed only by oxygen ion fluxes, Fig. 13 shows the current density profiles of the corresponding TCS configurations, which were obtained for the parameter of the electron pressure anisotropy outside the sheet of 5%: $\gamma_0 = (p_{e\parallel}(L) - p_{e\perp}(L))/p_{e\perp}(L) = 0.05$.

Figure 13a shows the configuration formed by proton fluxes with the parameters $T_p = 4$ keV and $\delta_p = 1.5$. The proton current $j_{py}(z)$ is shown with the brown line, electron current $j_{epy}(z)$, which is determined from Eq. (3.33), is shown with the violet line, and the total current $j_y(z) = j_{py}(z) + j_{epy}(z)$ is shown with the blue line. We note that the configuration with the same proton flux parameters, but with isotropic electrons, is shown in Figs. 2 and 3 with brown lines.

Figure 13b shows the configuration formed by the oxygen ion fluxes with the parameters $T_O = 0.4$ keV and $\delta_O = 5$. The oxygen ion current $j_{Oy}(z)$ is shown with the black line, electron current $j_{eOy}(z)$ with the blue line, and the total current $j_y(z) = j_{Oy}(z) + j_{eOy}(z)$ with the red line. For comparison, in Fig. 13a, the purple line shows the electron current $j_{epy}(z)$. We note that the configuration with the same parameters of the oxygen ion fluxes but with isotropic electrons, is shown in Fig. 8 with black lines. In both cases, the electrons transfer only a very small part of the total current through the sheet, which is determined by formula (3.15). For the TCS on protons, which is shown in Fig. 13a, the contribution of electrons to the magnetic field drop across the sheet was $\Delta B_e/\Delta B \approx 0.0026 = 0.26\%$. For the TCS on oxygen ions, which is shown in Fig. 13b, this contribution was $\Delta B_e/\Delta B \approx 0.0024 = 0.24\%$.

In both configurations, there is a very narrow strong positive electron current in the center of TCS, and wider zones with the negative electrons current adjoin it on both sides. In these zones, its minimum value is about 4–7 times less than its maximum value in the center of the CS. Moreover, in the case of the TCS on oxygen ions, these zones with the negative electron current are wider, and the maximum in the CS center is about 1.7 times larger. This difference, in accordance with Eqs. (3.33), is due to the difference in the profiles of the ion density and magnetic field.

Thus, within the spatially one-dimensional numerical model, in which the magnetized electrons are described by the Maxwell–Boltzmann distribution, electrons with the anisotropic pressure significantly redistribute the total current profile but provide a very small contribution to the total current through the CS.

We also note that the electron current peak at the CS center has been repeatedly detected in spacecraft measurements. In particular, such a peak was recently discovered in the TCS in the Martial magnetotail [33]. In this case it is quite possible that the aforementioned wider zones adjacent to it with a small negative electron current were also present, but were not detected against the background of the stronger positive ion

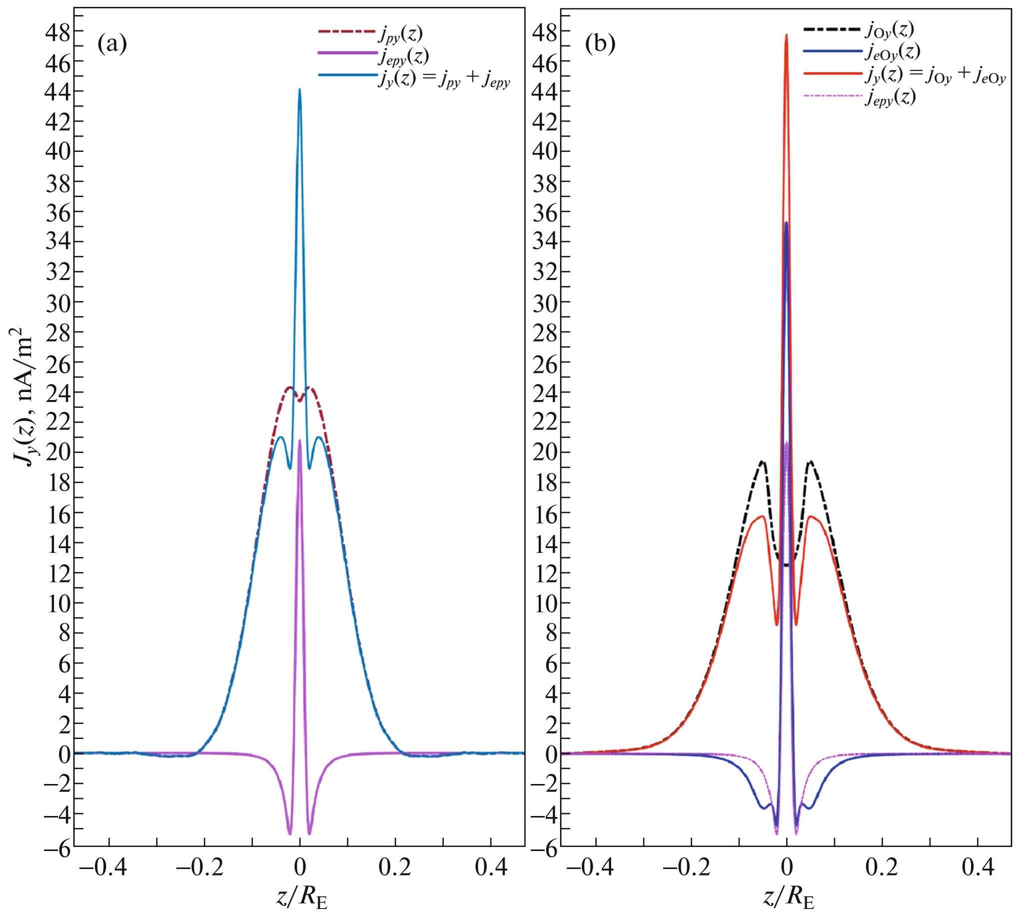

Fig. 13. Current density profiles of anisotropic electrons in the case of the electron pressure anisotropy at the edges of the sheet $\gamma_0 = (p_{e\parallel}(L) - p_{e\perp}(L))/p_{e\perp}(L) = 0.05$: (a) the configuration formed by proton fluxes with the parameters $T_p = 4$ keV and $\delta_p = 1.5$ (proton current $j_{py}(z)$—brown line, electron current $j_{epy}(z)$—violet line, total current $j_y(z) = j_{py}(z) + j_{epy}(z)$—blue line) and (b) the configuration formed by oxygen ion fluxes with the parameters $T_O = 0.4$ keV and $\delta_O = 5$. Oxygen ion current $j_{Oy}(z)$— black line, electron current $j_{eOy}(z)$—navy blue line, total current $j_y(z) = j_{Oy}(z) + j_{eOy}(z)$—red line, and electron current $j_{epy}(z)$—violet line.

current. The issue of a more accurate taking into account the counter electron fluxes in the model and the study of the electron current due to such fluxes requires further research.

8. DISCUSSION OF RESULTS AND CONCLUSIONS

This work describes a new version of the numerical model of a steady-state spatially one-dimensional TCS with a given normal component of the magnetic field, unmagnetized ions and magnetized electrons. Using this model, symmetric stationary TCS configurations of the near-Earth magnetotail were obtained in the growth phase of a substorm in a wide range of parameters of oncoming longitudinal proton and oxygen ion fluxes that form the CS. This made it possible to study the dependence of the TCS profiles on these parameters.

One can conclude from the simulation results that the formation of the TCS in the disturbed near-Earth magnetotail is possible due to the oxygen ion flows of the ionospheric origin, when the magnetospheric protons are either a background or their fluxes are relatively weak. In comparison with TCSs, which are formed only by proton flows, the configurations of TCSs that are formed by oxygen ion fluxes have a number of differences that can significantly affect their stability. In addition, the simulation results give estimates of the minimum velocity value of longitudinal proton and oxygen ion fluxes, which are necessary for the ion density profiles in the TCS to be within the observed range of $n_i < 1$ cm^{-3}.

The expression for the electron current density (3.12) is also obtained within the spatially one-dimensional model of the considered TCS. It follows from it that, first, the electron current density is nonzero only in the case of its pressure anisotropy, and, second, electrons make a nonzero contribution to the total current and the magnetic field drop in the CS only if their pressure at the CS edge has finite anisotropy. In the considered symmetric case, this contribution is given by formula (3.15) and is very small. In this case, the current density profile of anisotropic electrons in the center of CS has a very narrow strong positive peak, and wider zones with negative current adjoin it on both sides, in which its minimum value is several times lower than the maximum value in the center of the CS.

We note that the work presents the dependences of the distribution function of the population of current-carrying particles at the center of the CS as functions dimensionless velocity components in the coordinate system associated with the magnetic field. These plots demonstrate a clear dependence on the longitudinal hydrodynamic velocity of the flows forming the CS.

The following guidelines for the study of the data from satellite missions MMS, THEMIS, and CLUSTER on the CS intersection were elaborated. To present the distribution function at a given point of the CS, it is necessary to use dimensionless velocity components $\widetilde{V}_k = v_k / V^0_{T\alpha\perp}$ in a Cartesian coordinate system associated with the local magnetic field, in which the third axis is directed along the magnetic field at this point. As a scale for the velocity of particles of a given type α one should take their thermal speed $V^0_{T\alpha\perp}$ in a plane orthogonal to the magnetic field at the CS edge. For each plasma component, it is necessary to construct plots of distribution functions defined by formulas (4.3)–(4.6) at several points in the central region of the CS, and also at its edges. This makes it possible to identify the presence of counter longitudinal fluxes of each plasma component and to estimate their parameters.

For the further study of the issue of CS formation in the near-Earth magnetotail under disturbed conditions, a targeted analysis of the data from the MMS, THEMIS, and CLUSTER satellite missions is required in order to collect statistics on their intersection of the specified CS, to check for the presence of counter longitudinal proton, oxygen, ion, and electron fluxes in these data, and also to estimate the parameters of these fluxes. So, it is necessary to recover the profiles of the ion current density and the electron current density in the sheet using the ion and electron sensors, and also check the equality of the sum of the densities of the indicated currents of the total current density determined from the magnetic data.

CONFLICT OF INTEREST

The authors declare that they have no conflicts of interest.

REFERENCES

1. O. L. Vaisberg, L. A. Avanov, J. L. Burch, and J. H. Waite, Jr., Adv. Space Res. **18** (8), 63 (1996). https://doi.org/10.1016/0273-1177(95)00998-1
2. L. M. Kistler, C. Mouikis, E. Möbius, B. Klecker, J. A. Sauvaud, H. Rème, A. Korth, R. Marcucci, M. F. Lundin, G. K. Parks, and A. Balogh, J. Geophys. Res.: Space Phys. **110**, A06213 (2005). https://doi.org/10.1029/2004JA010653
3. L. M. Kistler, C. G. Mouikis, X. Cao, H. Frey, B. Klecker, I. Dandouras, A. Korth, M. F. Marcucci, R. Lundin, M. McCarthy, R. Friedel, and E. Lucek, J. Geophys. Res.: Space Phys. **111**, A11222 (2006). https://doi.org/10.1029/2006JA011939
4. E. A. Kronberg, M. Ashour-Abdalla, I. Dandouras, D. C. Delcourt, E. E. Grigorenko, L. M. Kistler, I. V. Kuzichev, J. Liao, R. Maggiolo, H. V. Malova, K. G. Orlova, V. Peroomian, D. R. Shklyar, Y. Y. Shprits, D. T. Welling, et al., Space Sci. Rev. **184**, 173 (2014). https://doi.org/10.1007/s11214-014-0104-0
5. E. A. Kronberg, D. Welling, L. M. Kistler, C. Mouikis, P. W. Daly, E. E. Grigorenko, B. Klecker, and I. Dandouras, J. Geophys. Res.: Space Phys. **122**, 9427 (2017). https://doi.org/10.1002/2017ja024215
6. L. M. Zelenyi, Kh. V. Malova, A. V. Artemyev, V. Yu. Popov, and A. A. Petrukovich, Plasma Phys. Rep. **37**, 118 (2011).
7. L. M. Zelenyi, Kh. V. Malova, E. E. Grigorenko, and V. Yu. Popov, Phys.—Usp. **59**, 1057 (2016).
8. D. N. Baker, E. W. Hones, Jr., D. T. Young, and J. Birn, Geophys. Res. Lett. **9**, 1337 (1982). https://doi.org/10.1029/GL009i012p01337
9. W. K. Peterson, R. D. Sharp, E. G. Shelley, R. G. Johnson, and H. Balsiger, J. Geophys. Res.: Space Phys. **86**, 761 (1981). https://doi.org/10.1029/JA086iA02p00761
10. R. D. Sharp, D. L. Carr, W. K. Peterson, and E. G. Shelley, J. Geophys. Res.: Space Phys. **86**, 4639 (1981). https://doi.org/10.1029/JA086iA06p04639
11. O. W. Lennartsson, J. Geophys. Res.: Space Phys. **99**, 2387 (1994). https://doi.org/10.1029/93JA03201
12. M. Nosé, A. T. Y. Lui, S. Ohtani, B. H. Mauk, R. W. McEntire, D. J. Williams, T. Mukai, and K. Yumoto, J. Geophys. Res.: Space Phys. **105**, 7669 (2000). https://doi.org/10.1029/1999JA000318
13. A. W. Yau, T. Abe, and W. K. Peterson, J. Atmos. Sol.-Terr. Phys. **69**, 1936 (2007). https://doi.org/10.1016/j.jastp.2007.08.010
14. A. V. Artemyev, A. A. Petrukovich, L. M. Zelenyi, R. Nakamura, H. V. Malova, and V. Y. Popov, Ann. Geophys. **27**, 4075 (2009). https://doi.org/10.5194/angeo-27-4075-2009
15. A. V. Artemyev, V. Angelopoulos, A. Runov, and X.-J. Zhang, J. Geophys. Res.: Space Phys. **125**, e2019-JA027612 (2020). https://doi.org/10.1029/2019JA027612
16. O. V. Mingalev, Kh. V. Malova, I. V. Mingalev, M. N. Mel'nik, P. V. Setsko, and L. M. Zelenyi, Plasma Phys. Rep. **44**, 899 (2018).

17. L. M. Zelenyi, H. V. Malova, V. Y. Popov, D. C. Delcourt, N. Y. Ganushkina, and A. S. Sharma, Geophys. Res. Lett. **33**, L05105 (2006). https://doi.org/10.1029/2005GL025117
18. V. I. Domrin, Kh. V. Malova, V. Yu. Popov, E. E. Grigorenko, and A. A. Petrukovich, Geomagn. Aeron. **60**, 173 (2020).
19. O. V. Mingalev, I. V. Mingalev, V. S. Mingalev, Kh. V. Malova, A. M. Merzlyi, and O. V. Khabarova, Plasma Phys. Rep. **46**, 374 (2020).
20. J. D. Huba, G. Joyce, and J. A. Fedder, J. Geophys. Res.: Space Phys. **105**, 23035 (2000).
21. J. D. Huba, G. Joyce, and J. Krall, Geophys. Res. Lett. **35**, L10102 (2008).
22. J. D. Huba, A. Maute, and G. Crowley, Space Sci. Rev. **212**, 731 (2017).
23. G. V. Khazanov, A. K. Tripathi, D. Sibeck, E. Himwich, A. Glocer, and R. P. Singhal, J. Geophys. Res.: Space Phys. **120**, 9891 (2015). https://doi.org/10.1002/2015JA021728
24. P. T. Newell, T. Sotirelis, and S. Wing, J. Geophys. Res.: Space Phys. **114**, A09207 (2009). https://doi.org/10.1029/2009JA014326
25. R. L. Lysak, J. Geophys. Res.: Space Phys. **109**, A07201 (2004). https://doi.org/10.1029/2004JA010454
26. L. I. Rudakov and R. Z. Sagdeev, in *Plasma Physics and the Problem of Controlled Thermonuclear Reactions,* Ed. by M. A. Leontovich (Pergamon, New York, 1959), Vol. 3, p. 321.
27. A. I. Morozov and L. S. Solov'ev, in *Reviews of Plasma Physics,* Ed. by M. A. Leontovich (Consultants Bureau, New York, 1968), Vol. 2, p. 201.
28. T. F. Volkov, in *Reviews of Plasma Physics,* Ed. by M. A. Leontovich (Consultants Bureau, New York, 1968), Vol. 4, p. 1.
29. R. M. Kulsrud, in *Basic Plasma Physics,* Ed. by A. A. Galeev and R. N. Sudan (North-Holland, Amsterdam, 1983), Vol. 1, p. 115.
30. V. I. Ilgisonis, Phys. Fluids B **5**, 2387 (1993). https://doi.org/10.1063/1.860722
31. L. M. Zelenyi, Kh. V. Malova, and V. Yu. Popov, JETP Lett. **78**, 296 (2003).
32. D. C. Delcourt, H. V. Malova, and L. M. Zelenyi, Geophys. Res. Lett. **33**, L06106 (2006). https://doi.org/10.1029/2005GL025463
33. E. E. Grigorenko, L. M. Zelenyi, G. DiBraccio, V. N. Ermakov, S. D. Shuvalov, H. V. Malova, V. Y. Popov, J. S. Halekas, D. L. Mitchell, and E. Dubinin, Geophys. Res. Lett. **46**, 6214 (2019). https://doi.org/10.1029/2019GL082709

Translated by L. Mosina